



UNIVERSITÀ DI PISA

Department of Physics
Masters Degree in Physics

Characterization of monolithic CMOS pixel sensors for charged particle detectors and for high intensity dosimetry

6 Candidate:
Ravera Eleonora

Supervisor:
Francesco Forti

7 Academic year 2021/2022

⁸ Contents

⁹ 1 TJ-Monopix1	3
¹⁰ 1.1 The sensor	4
¹¹ 1.2 Front end	6
¹² 1.2.1 ALPIDE-like	7
¹³ 1.3 Readout logic	8
¹⁴ 2 Arcadia-MD1	12
¹⁵ 2.1 The sensor and the front end	13
¹⁶ 2.2 Readout logic and data structure	14
¹⁷ 2.2.1 Matrix division and data-packets	14
¹⁸ 2.2.2 Matrix division and data-packets	15
¹⁹ 3 Characterization	18
²⁰ 3.1 TJ-Monopix1 characterization	18
²¹ 3.1.1 Threshold and noise: figure of merit for pixel detectors	18
²² 3.1.2 Linearity of the ToT	22
²³ 3.1.3 Calibration of the ToT	23
²⁴ 3.1.4 Changing the bias	28
²⁵ 3.1.5 Measurements with radioactive sources	29
²⁶ 3.1.6 Dead time measurements	34
²⁷ 3.2 ARCADIA-MD1 characterization	36
²⁸ 4 Test beam measurements	40
²⁹ 4.1 Apparatus description	41
³⁰ 4.1.1 Accelerator	41
³¹ 4.1.2 Mechanical carriers	41
³² 4.2 Measurements	42
³³ Bibliography	47

³⁴ **Chapter 1**

³⁵ **TJ-Monopix1**

³⁶ TJ-Monopix1 is a small electrode DMAPS with fast R/O capability, fabricated by Tow-
³⁷ erJazz foundry in 180 nm CMOS imaging process. It is part, together with prototypes
³⁸ from other series such as TJ-MALTA, of the ongoing R&D efforts aimed at developing
³⁹ DMAPS in commercial CMOS processes, that could cope with the requirements at ac-
⁴⁰ celerator experiments. Both TJ-Monopix and TJ-MALTA series [11], produced with the
⁴¹ same technology by TowerJazz (the timeline of the foundry products is shown in figure
⁴² 1.1), are small electrode demonstrators and principally differ in the readout design: while
⁴³ Monopix implements a column-drain R/O, an asynchronous R/O without any distribution
⁴⁴ of BCID has been used by TJ-Malta in order to reduce power consumption.



Figure 1.1: Timeline in TowerJazz productions in 180 nm CMOS imaging process

⁴⁵ Another Monopix series, but in 150 nm CMOS technology, has been produced by
⁴⁶ LFoundry [12]. The main differences between the LF-Monopix1 and the TJ-Monopix1
⁴⁷ (summarized in table 1.2), lay in the sensor rather than in the readout architecture, as
⁴⁸ both chips implements a fast column drain R/O with ToT capability [13][14]. Concerning
⁴⁹ the sensors, either are based on a p-type substrate, but with slightly different resistivities;
⁵⁰ in addition LFoundry pixels are larger, thicker and have a large fill factor (the very deep
⁵¹ n-well covers ~55% of the pixel area). The primary consequence is that LF-Monopix1
⁵² pixels have a higher capacity resulting in higher consumption and noise. As I discussed in
⁵³ section ??, the fact that LF-Monopix has a large fill factor electrode is expected to improve
⁵⁴ its radiation hardness. Indeed, a comparison of the performance of the two chips showed
⁵⁵ that TJ-Monopix suffers a comparatively larger degradation of efficiency after irradiation,
⁵⁶ due to the low electric field in the pixel corner; on the other hand, a drawback of the large
⁵⁷ fill factor in LF-Monopix is a significant cross-talk.

	LF-Monopix1	TJ-Monopix1
Resistivity	$>2 \text{ k}\Omega\text{cm}$	$>1 \text{ k}\Omega\text{cm}$
Pixel size	$50 \times 250 \mu\text{m}^2$	$36 \times 40 \mu\text{m}^2$
Depth	$100\text{-}750 \mu\text{m}$	$25 \mu\text{m}$
Capacity	$\sim 400 \text{ fF}$	$\sim 3 \text{ fF}$
Preamplifier	charge	voltage
Threshold trimming	on pixel (4-bit DAC)	global threshold
ToT	8 bits	6 bits
Consumption	$\sim 300 \text{ mW/cm}^2$	$\sim 120 \text{ mW/cm}^2$
Threshold	$1500 e^-$	$\sim 270 e^-$
ENC	$100 e^-$	$\sim 30 e^-$

Table 1.1: Main characteristics of Monopix1 produced by TowerJazz and LFoundry [13][14]

58 The TJ-Monopix1 chip contains, apart from the pixels matrix, all the required support
 59 blocks used for configuration and testing:

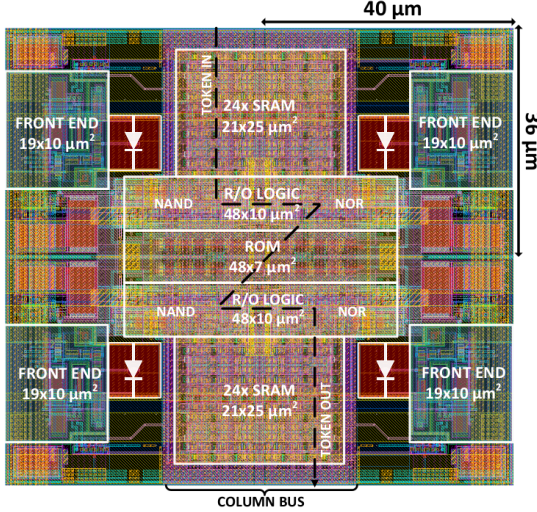
- 60 • the whole matrix contains 224×448 pixels, yielding a total active area approximately
 61 equal to 145 mm^2 over a total area of $1 \times 2 \text{ cm}^2$;
- 62 • at the chip periphery are placed some 7-bit Digital to Analog Converter (DAC), used
 63 to generate the analog bias voltage and current levels and to configuire the FE;
- 64 • at the EoC is placed a serializer to transferred datas immediately, indeed no trigger
 65 memory is implemented in this prototypes;
- 66 • the matrix power pads are distributed at the sides
- 67 • four pixels which have analog output and which can be monitored with an oscillo-
 68 scope, and therefore used for testing

69 Pixels are grouped in 2×2 cores (fig. 1.2a): this layout allows to separate the analog
 70 and the digital electronics area in order to reduce the possible interference between the
 71 two parts. In addition it semplifies the routing of data as pixels on double column share
 72 the same column-bus to EoC. Therefore pixels can be addressed through the physical
 73 column/row or through the logical column/row, as shown in fig. 1.2b: in figure is also
 74 highlighted the token propagaion path, whose I will discuss later.

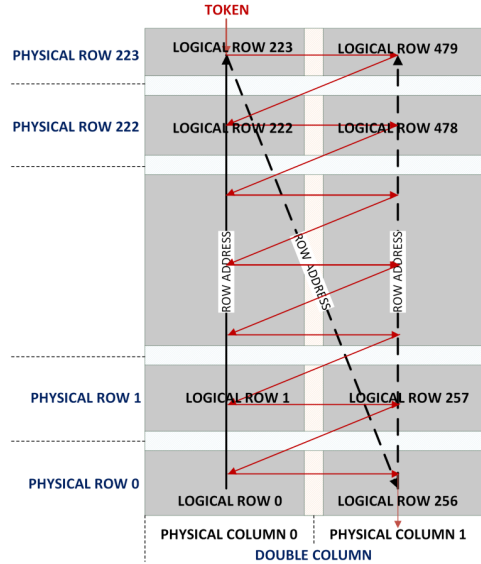
75 Concerning the integration2.3 of the chip in a readout path, TJ-Monopix1 chips have
 76 been wire-bonded on a dedicated carrier board , the Printed Circuit Board (PCB). Two
 77 other board between the DAQ and the chip: the General Purpose Analog Card (GPAC),
 78 which provides power supply channels, current/voltage bias sources and I/O buffer, and
 79 the MIO3 FPGA, which strictly interacts with the DAQ.

80 1.1 The sensor

81 As already anticipated, TJ-Monopix1 has a p-type epitaxial layer and a n doped small
 82 collection electrode ($2 \mu\text{m}$ in diameter); to avoid the n-wells housing the PMOS transistors
 83 competing for the charge collection, a deep p-well substrate, common to all the pixel FE



(a) Layout of a core containing 4 pixels. The analog FE and the digital part are separated in order to reduce cross-talk be



(b)

Parameter	Value
Matrix size	$1 \times 2 \text{ cm}^2$
Pixel size	$36 \times 40 \mu\text{m}^2$
Depth	$25 \mu\text{m}$
Electrode size	$2 \mu\text{m}$
BCID	40 MHz
ToT-bit	6
Power consumption	$\sim 120 \text{ mW/cm}^2$

Table 1.2

area, is used. TJ-Monopix1 adopts the modification described in section ?? that allows to achieve a planar depletion region near the electrode applying a relatively small reverse bias voltage. This modification improves the efficiency of the detector, especially after irradiation, however a simulation of the electric field in the sensor, made with the software TCAD (Technology Computer Aided Design), shows that a nonuniform field is still produced in the lateral regions of the pixel compromising the efficiency at the corner. Two variations to the process have been proposed in order to further enhance the transversal component of electric field at the pixel borders: on a sample of chip, which includes the one in Pisa, a portion of low dose implant has been removed, creating a step discontinuity in the deep p-well corner (fig. 1.3); the second solution proposed[MOUSTAKAS THESY, PAG 58] consists in adding an extra deep p-well near the pixel edge. A side effect of the alteration in the low dose implant is that the separation between the deep p-well and the p-substrate becomes weak to the point that they cannot be biased separately to prevent the punchthrough.

Moreover, to investigate the charge collection properties, pixels within the matrix are split between bottom top half and bottom half and feature a variation in the coverage of the deep p-well: the electronics area can be fully covered or not. In particular the pixels

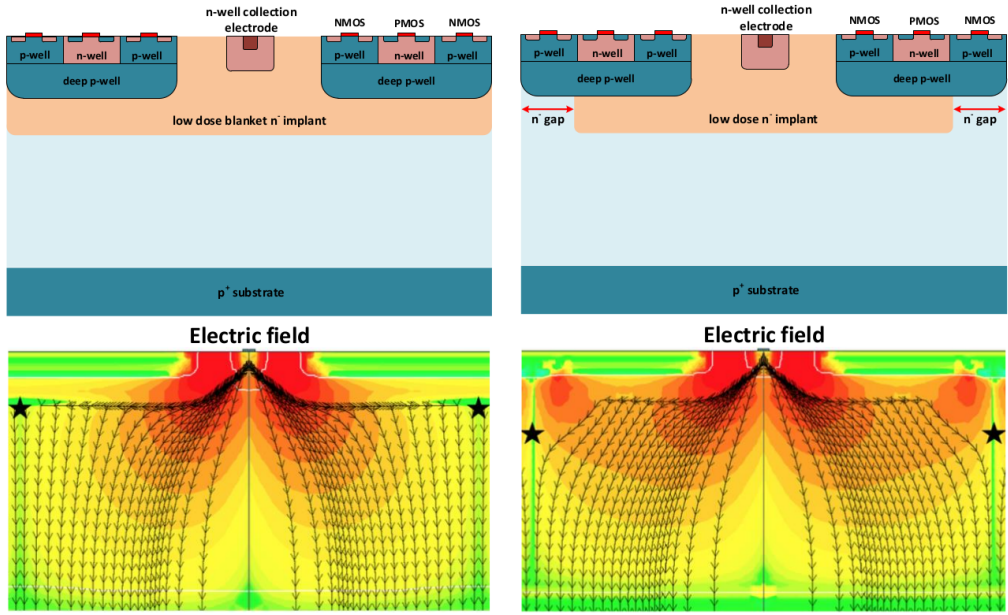


Figure 1.3: (a) The cross-section of a monolithic pixel in the TJ-Monopix with modified process; additionally in (b) a gap in the low dose implant is created to improve the collection of charge due to a bigger lateral component of the electric field. this point in figure is indicated by a star . transversal component of the electric field drops at the pixel corner

101 belonging to rows from 0 to 111 are fully covered (FDPW) and pixels belonging to rows
 102 from 112 to 223 have a reduced p-well (RDPW), resulting in a enhancement of the lateral
 103 component of the electric field.

104 1.2 Front end

105 One of the main advantage of this chip is the small collection electrode, which results in a
 106 small capacitance ($C_{in}=3\text{ fF}$) allowing for high input signal amplitude and single stage of
 107 amplification, which obviously improves the signal to noise ratio performance of the FE.
 108 Assuming a fully depleted epitaxial layer of $25\text{ }\mu\text{m}$, which corresponds approximately to
 109 a $20\text{ }\mu\text{m}$ of deep sensing volume, a MIP should produce $\sim 1600\text{ e}^-$, then:

$$V_{in} = \frac{1600\text{ e}^- \times 1.6 \cdot 10^{-19}\text{ C}}{3\text{ fF}} = 85\text{ mV} \quad (1.1)$$

110 Secondly, a reset mechanism which slowly discharges the detector capacitance must be
 111 included in the circuit:

$$V_{in} = \frac{Q_s}{C_{in}} e^{-t/R_b C_{in}} \quad (1.2)$$

112 where R_b is the equivalent reset element. The general constraint which must be satisfied
 113 is that the discharge time $\tau = R_b C_{in}$ must be slower than the characteristic time of
 114 the amplifier, otherwise a signal loss could occurs. Traditionally the reset can be
 115 implemented in two different way: with a forward biased diode, that might be implemented
 116 by a simple p+ diffusion inside the well of the collection electrode n, or with a PMOS
 117 transistor. Despite of the semplicity of the diode reset, since it is a non-linear element,
 118 the discharge would depend on the quantity of charge Q generated on the n electrode,

119 prejudicing the linearity of the analog output (Q-ToT). To solve the issue, a PMOS reset
 120 is the method preferred in design such TJ-Monopix1 with analog output; the PMOS
 121 transistor, indeed, can acts as a constant current source and then used to discharge the
 122 sensor. Although the PMOS reset is capable of providing a constant current, it has to be
 123 manually re-tuned every time in order to restore the input DC baseline voltage; to do that
 124 a low-frequency feedback is used.

125 The matrix is split in four sections, each one corresponding to a different flavor of the
 FE, implemented in order to test more options.

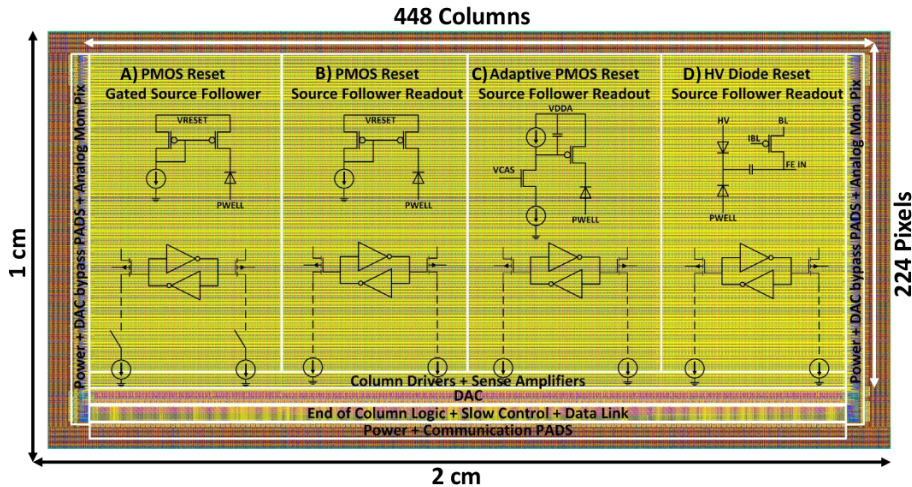


Figure 1.4: TJ-Monopix1 has been developed in four different flavor. The flavor PMOS reset (B) is considered as the reference one.

126
 127 All the flavors implement a source-follower double-column bus readout: the standard
 128 variation is the flavor B, that features a PMOS input reset (refered as "PMOS reset").
 129 Flavor A is identical to flavor B except for the realization of the source follower (it is a
 130 gated one): in the circuit of the gated versione there is a transistor more that operates on
 131 the baseline and on the feedback mechanism; this aim to reduce the power consumption
 132 and results in a higher signal baseline, and then in a lower effective threshold. C instead
 133 implements a novel leakage compensation circuit, with a PMOS reset configuration. More-
 134 over the collection electrode can be either DC-coupled to the readout electronics, as in
 135 flavors A, B, C, or AC-coupled through a metal-oxide-metal (MOM) capacitor, as in D
 136 is AC-coupled. The latter one allows applying a high bias voltage to the electrode n and
 137 for this reason the flavor D is also called "HV flavor". Unfortunately the "HV" suffer
 138 from a signal loss, which can achieve even the 50%, due to the additional parasitic capac-
 139 ity introduced at the input node. The HV voltage above which the breakdown begins is
 140 ~ 50 V; however at values bigger than 20 V, the gain does not increase anymore, since the
 141 depletion zone is already fully depleted.

142 1.2.1 ALPIDE-like

143 ALPIDE chips, developed by the ALICE collaboration, implemented a standard FE to the
 144 point that many CMOS MAPS detectors used a similar FE and are called "ALIPDE-like".
 145 Considering that both TJ-Monopix1 and ARCADIA-MD1 have an ALPIDE-like FE, I am
 146 going to explain the broad principles of the early FE stage. The general idea is of the
 147 amplification to transfer the charge from a bigger capacity[15], C_{source} , to a smaller one,

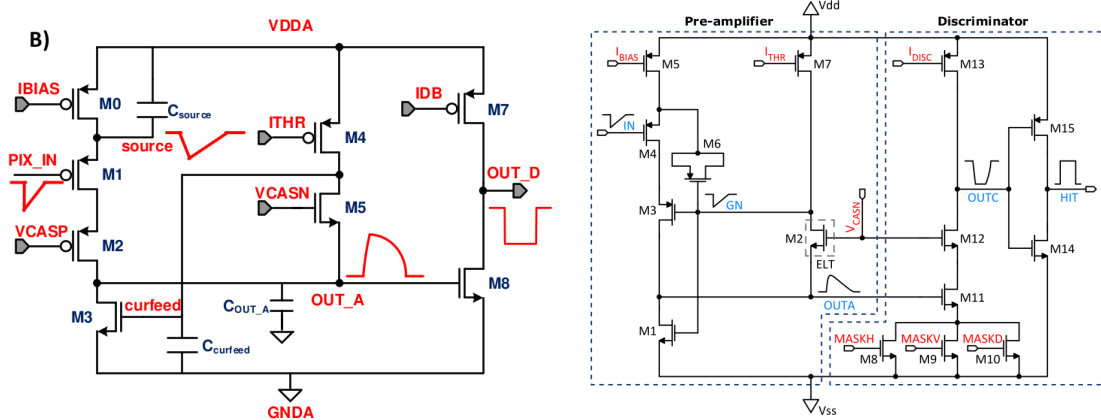


Figure 1.5

¹⁴⁸ C_{out} : the input transistor M1 with current source IBIAS acts as a source follower and this
¹⁴⁹ forces the source of M1 to be equal to the gate input $\Delta V_{PIX_IN} = Q_{IN}/C_{IN}$.

$$Q_{source} = C_{source} \Delta V_{PIX_IN} \quad (1.3)$$

¹⁵⁰ The current in M2 and the charge accumulates on C_{out} is fixed by the one on C_{source} :

$$\Delta V_{OUT_A} = \frac{Q_{source}}{C_{OUT_A}} = \frac{C_{source} \Delta V_{PIX_IN}}{C_{OUT_A}} = \frac{C_{Source}}{C_{OUT_A}} \frac{Q_{IN}}{C_{IN}} \quad (1.4)$$

¹⁵¹ A second branch (M4, M5) is used to generate a low frequency feedback, where VCASN
¹⁵² and ITHR set the baseline value of the signal on C_{OUT_A} and the velocity to goes down
¹⁵³ to the baseline. **IL RUOLO DI CURVFEED NON L'HO CAPITO.** Finally IDB defines
¹⁵⁴ the charge threshold with which the signal OUT_A must be compared: depending on if
¹⁵⁵ the signal is higher than the threshold or not, the OUT_D is high or low respectively.

¹⁵⁶ The actual circuit implemented in TJ-Monopix1 is shown in figure 1.5: the principal
¹⁵⁷ difference lays in the addition of disableing pixels' readout. This possibility is uttermost
¹⁵⁸ important in order to reduce the hit rate and to avoid saturating the bandwidth due to the
¹⁵⁹ noisy pixels, which typically are those with manufacturing defects. In the circuit transis-
¹⁶⁰ tors M8, M9 and M10 have the function of disabling registers with coordinates MASKH,
¹⁶¹ MASKV and MASKD (respectively vertical, orizontal and diagonal) from readout: if all
¹⁶² three transistors-signals are low, the pixel's discriminator is disabled. Compared with a
¹⁶³ configurable masking register which would allow disableing pixels individually, to use a
¹⁶⁴ triple redundancy reduces the sensistivity to SEU but also gives amount of intentionally
¹⁶⁵ masked ("ghost") pixels. This approach is suitable only for extremely small number N of
¹⁶⁶ pixel has to be masked: if two coordinate projection scheme had been implemented, the
¹⁶⁷ number of ghost pixels would have scale with N^2 , if instead three coordinates are used,
¹⁶⁸ the N's exponential is lower than 2 (fig. 1.6)

¹⁶⁹ Foto dell'oscilloscopio per far vedere cosa fanno i parametri

¹⁷⁰ 1.3 Readout logic

¹⁷¹ TJ-Monopix1 has a triggerless, fast and with ToT capability R/O which is based on a
¹⁷² column-drain architecture. On the pixel are located two Random Access Memory (RAM)
¹⁷³ cells to store the 6-bit LE and 6-bit TE of the pulse, and a Read-Only Memory (ROM)

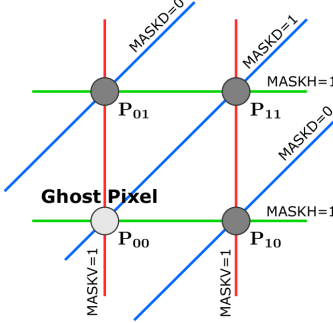


Figure 1.6

Parameter	Meaning	
IBIAS	mainly controls the rise time	yes
IDB	sets the discriminator threshold	yes
ITHR	sets the velocity of the return to the baseline	yes
ICASN	sets the baseline of the signal	yes
VRESET	sets the gain of the preamplifier	yes
IRESET	sets the gain of the preamplifier	no

Table 1.3: FE parameters which must be setted through the DAQ. "Function" means that higher parameter implies higher value

174 containing the 9-bit pixel address. Excluded these memories, TJ-Monopix1 hasn't any
 175 other buffer: if a hit arrives while the pixel is already storing a previous one, the new
 176 data get lost. After being read, the data packet is sent to the EoC periphery of the
 177 matrix, where a serializer transfers it off-chip to an FPGA (1.7). There a FIFO is used
 178 to temporarily stored the data, which is transmitted to a computer through an ethernet
 179 cable in a later time.

180 The access to the pixels' memory and the transmission of the data to the EoC, following
 181 a priority chain, is managed by control signals and is based on a Finite State Machine
 182 (FSM) composed by four state: no-operation (NOP), freeze (FRZ), read (RD) and data
 183 transfer (DTA). The readout sequence (??) starts with the TE of a pulse: the pixel
 184 immediately tries to grab the column-bus turning up a hit flag signal called *token*. The
 185 token is used to control the priority chain and propagates across the column indicating
 186 what pixel that must be read. To start the readout and avoid that the arrival of new hits
 187 disrupt the priority logic, a *freeze* signal is activated, and then a *read* signal controls the
 188 readout and the access to memory. During the freeze, the state of the token for all pixels
 189 on the matrix remains settled: this does not forbid new hits on other pixels from being
 190 recorded, but forbids pixels hit from turning on the token until the freeze is ended. The
 191 freeze stays on until the token covers the whole priority chain and gets the EoC: during
 192 that time new token cannot be turned on, and all hits arrived during a freeze will turn
 193 on their token at the end of the previous freeze. Since the start of the token is used to
 194 assign a timestamp to the hit, the token time has a direct impact on the time resolution
 195 measurement; this could be a problem coping with high hits rate.

196 The analog FE circuit and the pixel control logic are connected by an edge detector
 197 which is used to determine the LE and the TE of the hit pulse(fig. 1.9): when the TE

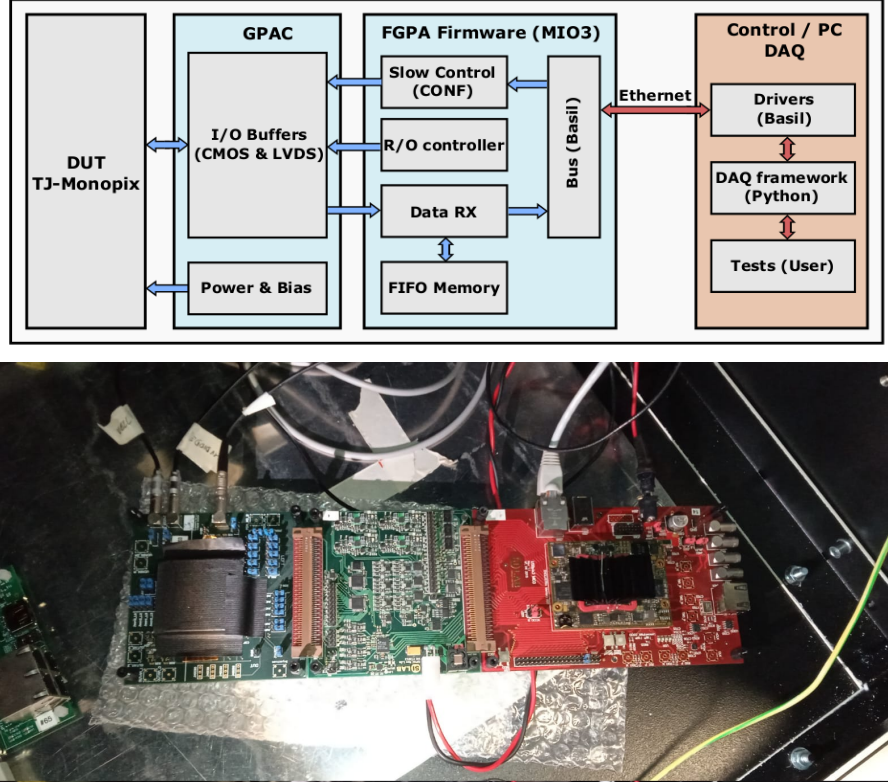


Figure 1.7: Main caption

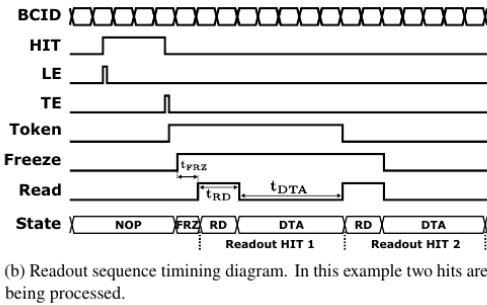


Figure 1.8: Readout timing diagram: in this example two hits are being processed

198 is stored in the first latch the edge detector is disabled and, if the **FREEZE** signal is not
 199 set yet, the readout starts. At this point the **HIT** flag is set in a second latch and a token
 200 signal is produced and depending on the value of **Token** in the pixel can be read or must
 201 wait until the **Token in** is off. In figure an OR is used to manage the token propagation, but
 202 since a native OR logic port cannot be implemented with CMOS logic, a sum of a NOR
 203 and of an inverter is actually used; this construct significantly increases the propagation
 204 delay (the timing dispersion along a column of 0.1-0.2 ns) of the token and to speed up
 205 the circuit optimized solution are often implemented. When the pixel become the next to
 206 be read in the queue, and at the rising edge of the **READ** signal, the state of the pixel is
 207 stored in a D-latch and the pixel is allowed to use the data bus; the **TE** and the **HIT** flag
 208 latches are reset and a **READINT** signal that enable access of the RAM and ROM cells
 209 is produced.

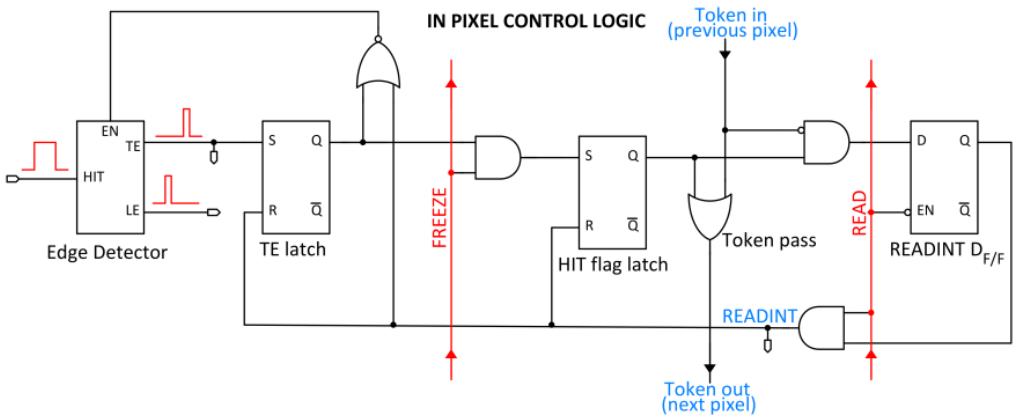


Figure 1.9

210 The final data must provide all the hits' information: the pixel address, the ToT and
 211 the timestamp. All those parts are assigned and appended at different time during the
 212 R/O chain:

- 213 • **Pixel address:** while the double column address (6-bit) is appended by the EoC
 circuit, the row address (8-bits for each flavor) and the physical column in the doublet
 (1-bit) are assigned by the in-pixel logic
- 216 • **ToT:** is obtained offline from the difference of 6-bits TE and 6-bits LE, stored by
 the edge detector in-pixel; since a 40 MHz BCID is distributed across the matrix,
 the ToT value is range 0-64 clock cycle which corresponds to 0-1.6 μ s
- 219 • **Timestamp:** The timestamp of the hit correspond to the time when the pixel set
 up the token; it is assigned by the FPGA, that uses the LE, TE and a 640 MHz
 clock to derive it. For all those hits which arrived while the matrix is frozen, the
 timestamp is no more correlated with the time of arrival of the particle

223 When the bits are joined up together the complete hit data packet is 27-bit.

224 **Chapter 2**

225 **Arcadia-MD1**

226 [16] [17]

227 ARCADIA (Advanced Readout CMOS Architectures with Depleted Integrated sensor
228 Arrays) and SEED (Sensor with Embedded Electronic Developement) are both groups
229 involved in the development of MAPS sensors based on the CMOS technology and both
230 having LFoundry as industrial partner. Many concept and performances studies have been
231 carried out with simulations and small-scale test structure by SEED, before ARCADIA,
232 applying the experience developed with SEED to a full chip prototype, the MD1. MA-
233 TISSE is an example of small-scale prototypes produced for testing: it is made by 24×24
234 pixels organised in 4 columns; each pixel has an analog output, which allows for energy
235 loss measurements, and a shutter snapshot readout with a speed that can reach 5 MHz.

236 The ARCADIA target are the development of a novel CMOS sensor platform allowing
237 for fully depleted active sensors with thickness in range $50 \mu\text{m}$ to $500 \mu\text{m}$. A small charge
238 collecting electrode to achieve a good signal to noise ratio, a high time resolution (the
239 lower bound is set at $O(\mu\text{m})$ but more advanced solutions are investigating for a $O(10 \text{ ns})$)
240 and a scalable readout architecture with low power consumption are the main requirement
241 imposed by ARCADIA; the Main Demonstrator 1, has been submitted in 2020, and its
242 characteristic are shown in table 2.1. A second main demonstrator (ARCADIA-MD2) has
243 been submitted in Summer 2021, featuring a similar design of MD1 and which is expected
244 to be faster and to have a lower power consumption thanks to a logic and buffering
245 optimisation.

Parameter	Value
Matrix size	$\times \text{ cm}^2$
Pixel size	$25 \times 25 \mu\text{m}^2$
Depth	$48/100/200 \mu\text{m}$
Electrode size	$9 \times 9 \mu\text{m}^2$
Power consumption	$\sim 10 \text{ mW/cm}^2$

Table 2.1

246 2.1 The sensor and the front end

247 ARCADIA-MD1 is an LFoundry chip which implements the CMOS technology in 110 nm
 248 ???. The standard p-type substrate is replaced by a n-type ???

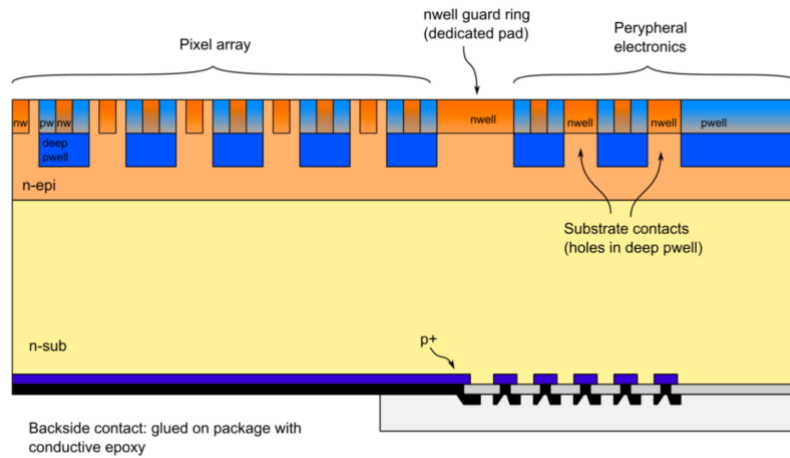


Figure 2.1

249 The sensor is made by a *p* substrate and an *n* doped diode within a *n* epitaxial layer.
 250 Being part of DMAPS category, it is operated in fully depletion and the charge is then
 251 fastly collected by drift. Up to now the sensor has been implemented in three different
 252 variant: 48 μm , 100 μm and 200 μm thick, each with the same FE and readout logic but
 253 requiring a diffent biasing.

254 MD1 chips have been submitted in two different front end options: they are commonly
 255 called ALIPDE-like and bulk-driven. The differences between them are in the FE circuit
 256 and in the biasing current of the registers, while the underlying readout is the same.
 257 The main difference is in the amplification stage, while in the ALPIDE-like flavor the
 258 amplification is implemented as explained in section 1.2.1, in the bulk-driven flavor the
 259 gain is adjusted by the ratio of two transconduttances. Consequently, some of the biasing
 260 registers, whose current is settable externally by the DAQ, have different default values
 261 and they might not be available at all in one of the flavor. An example is the ICLIP
 262 register, which is available only in the bulk driven flavor despite the transistor to which
 263 refers is implemented in both the flavor; its function is similar to the *curfeed* capacitor in
 264 figure 1.5(a), which controls the current in the input branch of the FE and also influences
 265 the value of tha baseline at the discriminator input.

266 There are three types of configuration registers which are used to configure the matrix:

- 267 • the Pixel Configuration Register, which is a 2-bits word used for enableing respec-
 268 tively the masking and injection functionalities. The on pixel Pixel Configuration
 269 Register circuit and how the mask/injection can be enable/disable is shown in figure
 270 2.2.
- 271 • the Internal Configuration Register, which are used for the communication with the
 272 FPGA, for example to send a pulse, reset or configure the whole matrix.
- 273 • the Global Configuration Registers, which are used to set the configuration of the
 274 FE parameters are similar to the one of the TJ-Monopix1 circuit.

275 Their bias with the one of the sensors are supplied by padframes (a top, a bottom and a
 276 side one) placed aside the matrix, which also provide the clock, the reset, the test pulse
 for the injection circuit and the communication signals.

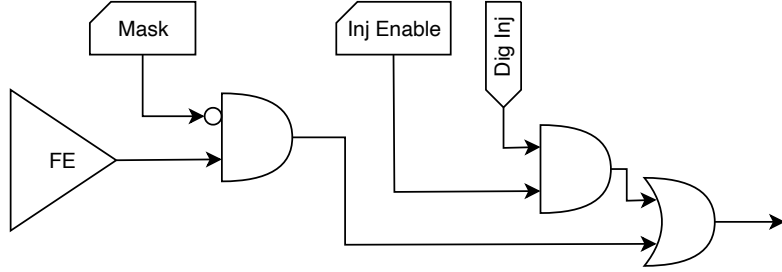


Figure 2.2

277

278 2.2 Readout logic and data structure

279 2.2.1 Matrix division and data-packets

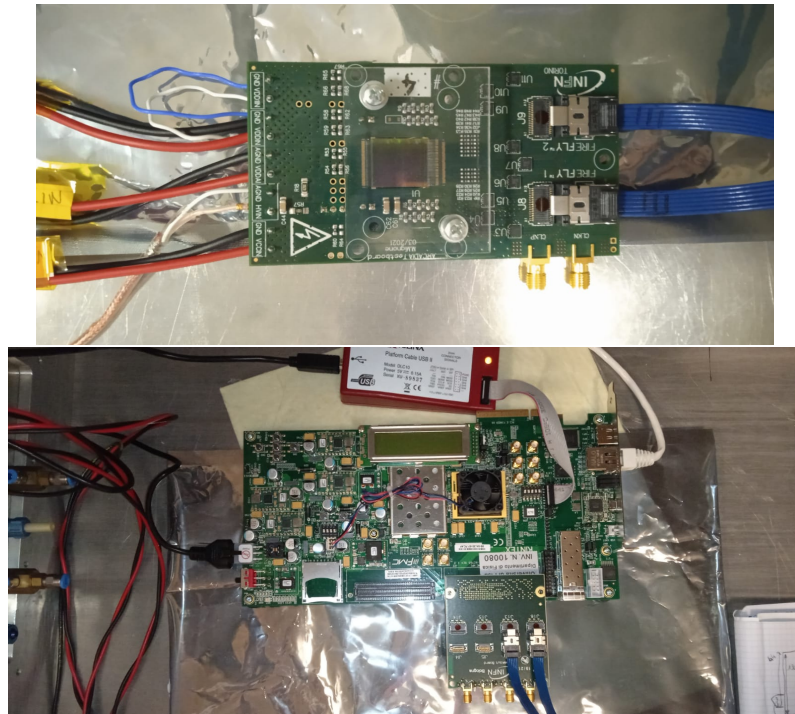


Figure 2.3: (a) Board hosting the MD1 and (b) FPGA

280 One of the main ambition of the MD1 is to achieve the lowest possible power consump-
 281 tion, hopefully less than 20 mW/cm^2 ; this is principally due to the hope of application also
 282 in space experiment field, where the power consumption and the cooling are for sure an
 283 issue. In order to undergo that requirement, the matrix is clockless and the readout is
 284 triggerless; moreover the chip can be operated both in the high rate mode and low rate
 285 depending on if only one or all serializers, which are placed at the periphery of the matrix
 286 are enabled or only one is shared between the sections; in addition, to save as much area
 287 as possible, no buffer have been included on the matrix at the expense of the maximum

Bits	Meaning
31:24	timestamp
23:20	section index
19:16	column index
15:9	pixel region
8:0	bitmap

Table 2.2: Data packet structure implemented by the MD1 readout logic.

288 hit rate sustainable. The readout then is completely data push and when a hit is received
 289 immediately starts the readout mechanism to transmit it off chip.

290 The board hosting the chip is connected with a breakout board, which is connected to
 291 the FPGA; a data packet sent to the EoS, is then encoded and transmitted to the FPGA
 292 using a 320 MHz DDR serializers and then transmitted by ethernet to the PC. A photo of
 293 the experimental setup is shown in figure ??.

294 2.2.2 Matrix division and data-packets

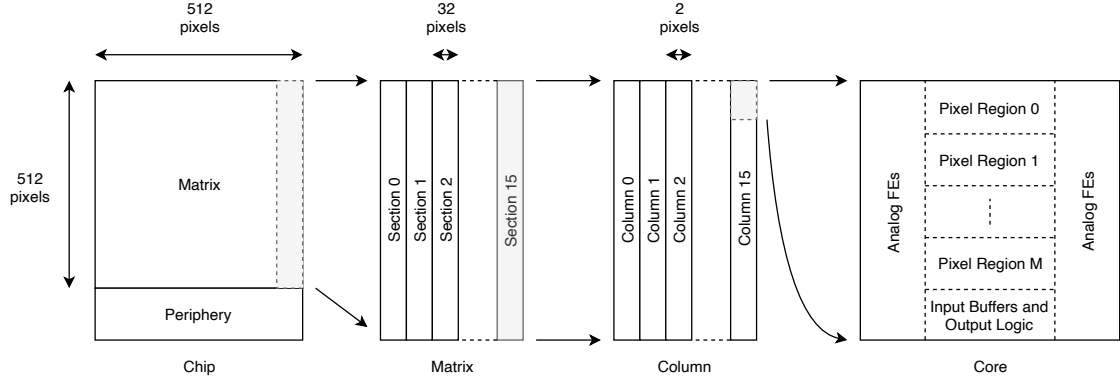


Figure 2.4

295 Also the chip structure is meant to optimize the power consumption and the scalability
 296 for future up-scaling; in particular it is divided into a physical and logical hierarchy, which
 297 also reflects in the way the data packets are built (tab.2.2). First of all, the 512 columns
 298 are split in 16 sections each one containing 512×32 pixels and having its own biasing lines
 299 and serializers at the matrix periphery. Each section is divided into 512×2 double-column
 300 mirrored, which just as in TJ-Monopix1, share the same readout buses placed between
 301 them and having analog logic on the sides. The rows, then, are divided in groups of 32,
 302 resulting in core with 32×2 pixels. Finally each core is sub-divided in regions, each one
 303 containing 4×2 pixels.

304 The readout has been designed with the constraints of being capable of handling with
 305 hit rate of $100 \text{ MHz}/\text{cm}^2$, then it has been optimized to minimize the amount of logic and
 306 to have a high bandwidth of transmission of the data to the periphery. For this reason not
 307 all pixels have been provided by the readout logic. In particular, each pixel region can
 308 either be Master or Slave, depending on if it has or has not the readout capability. The
 309 Master's data packets are therefore composed of two parts: the bitmap of the Master
 310 itself and the one of Slave. Moreover, the pioneer idea of ARCADIA-MD1, which has as

311 finally goal the test of a readout cabable of transmit cluster data in as few data packets
 312 as possible, is the possibility of the Master to decide what Slave (top or bottom) read; the
 313 information of what Slave has been selected is represented by a bit, often called *hot bit*, in
 314 the data-packet. Every pixel has an associated status register, that essentialaly is a flip flop
 315 (FF), which is set to 1 when the pixel stores a hit; an OR of the FF whithin the Master
 316 or the Slave region generates an active flag which is used to require a readout by the EoS.
 In figure 2.5 is shown the circuit with the logic of assignment of the Slave to the Master.

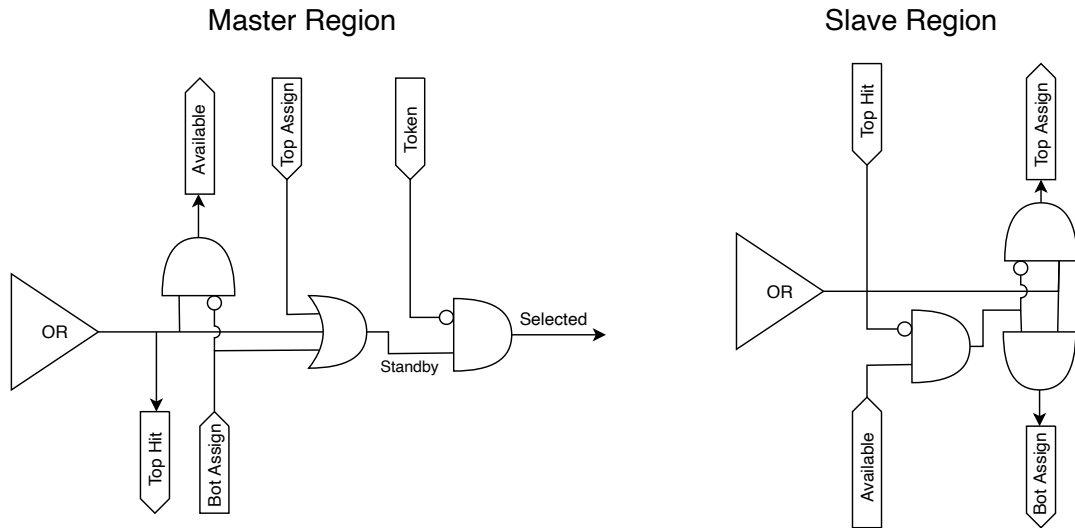


Figure 2.5

Depending on the active flags of the neighbouring Masters, the Slave bitmap is assigned to the one at the top or bottom. If both the Masters have an active flag, the Slave is assigned to the top one. In the example in figure 2.6 two Master-Slave regions are considered: the bitmaps of the Master (red colored in the example) and Slave (blue colored) are joined together within a unique data packet and a bit (green colored) is used to specify the Slave.

The data packets are transmitted to the End of Section (EoS) with a priority chain similar to what happens in TJ-Monopix1. If at least one Master set a high flag, a **Token** signal is generated and is assigned to the high priority Master in the column, together with a **Full** flag which is distributed to the active Masters in the whole column in order to deny more region to be accessed at the same time. The readout then propagates down the column from Master to Master, skipping the empty cores; the Master selected for the readout is the one with the flag high and with an input (from top) **Token** equal to 0. In the example in figure 2.7 the **Token** is propagated from the Pixel Region (PR) 10 to the PR 7. In the three readout steps the red Masters are the ones selected for the readout, while the yellow are the ones which an active flag high; gray color is used for empty regions. When a specific Master has been selected, a **Read** signal is generated both to transmit the data to the EoS and also to generate a reset for the just read pixels. Once the pixels are reset, the Master's **Full** and **Token** flags fall, and the following region which satisfies the two readout conditions explained above, becomes selected.

The performances of the readout has been studied with simulations by the designer of the chip. Random hits events with cluster size of 4 pixels on average, with a Poissonian distribution in time and uniformly distributed on the matrix has been generated.

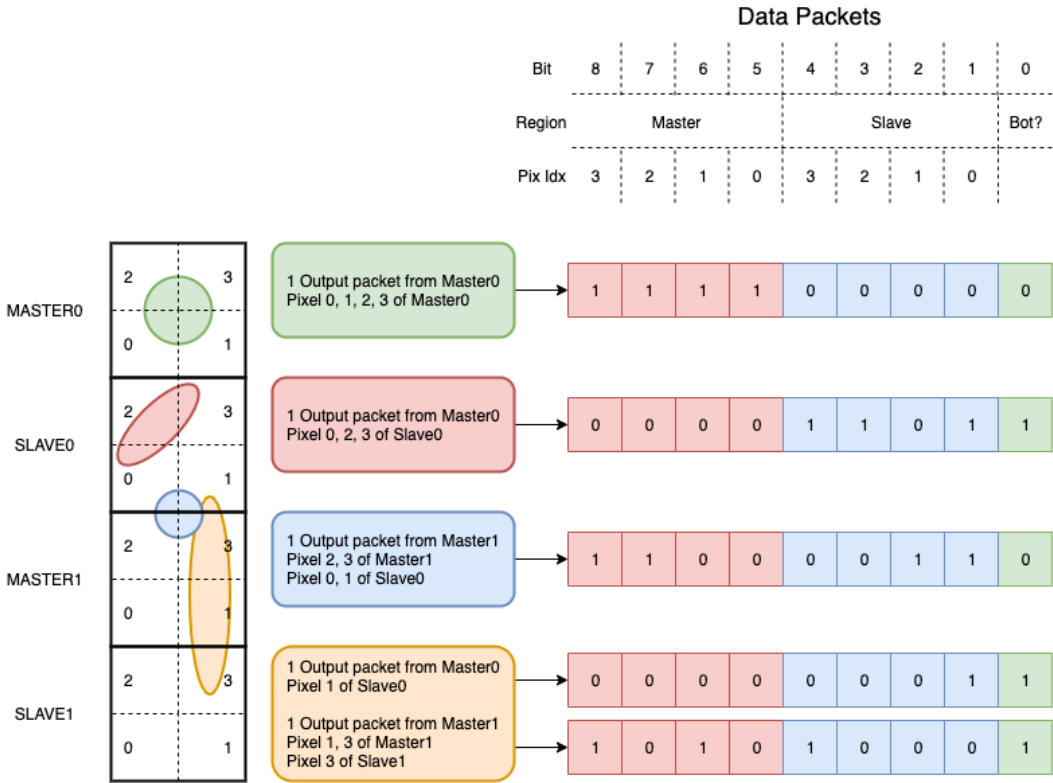


Figure 2.6: Different cluster structures and the data packet produced by them are shown in the example.

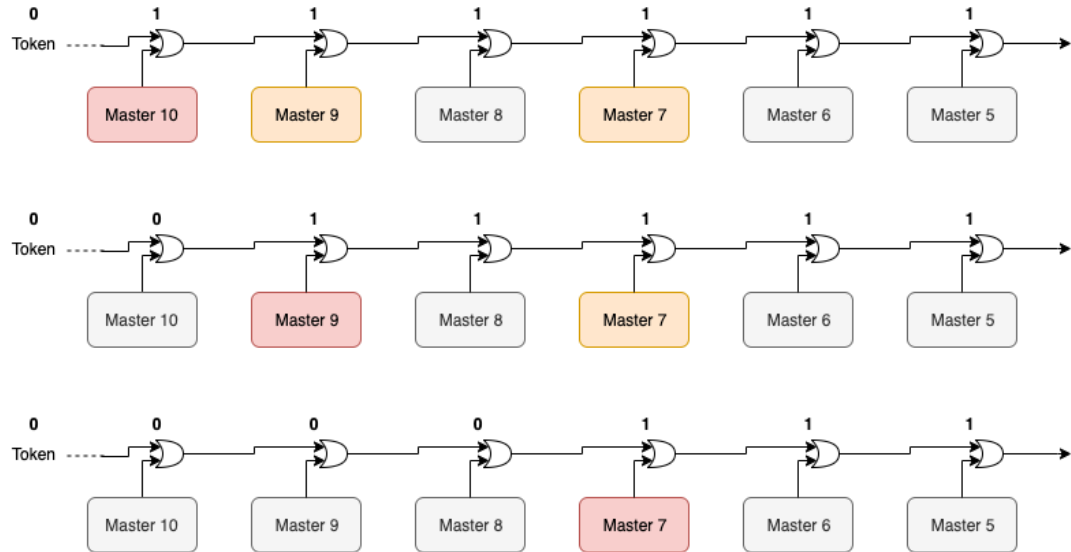


Figure 2.7

³⁴¹ They state that with particle hit rate of 100 MHz/cm², considering a portion of matrix of
³⁴² three section (512×96), the efficiency results to be 98.7%, while reducing the hit rate to
³⁴³ 80 MHz/cm² it is even higher achieving the 99.95%.

344 **Chapter 3**

345 **Characterization**

346 Rifai il conto della lunghezza di attenuazione. Ho trovato (presentazione Luciano Mus) 29
347 um per ka e 37 um per kb.

348 **3.1 TJ-Monopix1 characterization**

349 **3.1.1 Threshold and noise: figure of merit for pixel detectors**

350 A characterization of threshold and noise is typically necessary since these values have an
351 impact on the operating conditions and on the performance of the chips, so much that
352 the signal to threshold ratio may be considered as the figure of merit for pixel detectors
353 rather than the signal to noise ratio. The mean minimum stable threshold evolved through
354 different generation of chips: in the 1st generation it was around 2500 e^- while in the 3rd
355 (corresponding to nowadays chips) is less than 500 e^- . This allows in thinner sensors with
356 smaller signals: from $16\,000 \text{ e}^-$ produced in $200 \mu\text{m}$, the signal expected moved down to
357 2000 e^- produced in $25 \mu\text{m}$. In agreement with this, the threshold of TJ-Monopix1 is
358 around 500 e^- .

359 Obviously the threshold has to be located between the noise peak around the baseline
360 and the signal distribution, in particular it has to be low enough to mantain a high signal
361 efficiency, but also high enough to cut the noise: for a low threshold many pixels can fire
362 at the same time and a positive feedback can set off a chain reaction eventually, causing
363 all the other pixels to fire. Thus, the noise sets a lower bound to the threshold: if an
364 occupancy $\leq 10^{-4}$ is required, for example, a probability of firing lower than that value
365 is needed and this, assuming a gaussian noise, requires that the threshold is set at least
366 3.7σ , with σ the RMS of the noise. In this case, if the noise is 100 e^- (resonable), the
367 threshold must be higher than $3.7 \times 100 \text{ e}^-$. Typically this argument sets only a minimal
368 bound to the threshold since the variation with time and from pixel to pixel have to be
369 taken into account: the temperature, the annealing (for example, the radiation damages in
370 the oxide layer causes shift of MOSFET threshold voltage) and the process parameters
371 variation across the wafer (as for example process mismatch between transistors).

372 On the other hand, concerning the noise, given that the first stage of amplification is
373 the most crucial, since in the following stages the signal amplitude is high compared to
374 additional noise, it is valued at the preamplifier input node. Then, the noise is parame-
375 terized as Equivalent Noise Charge (ENC), which is defined as the ratio between the noise
376 N at the output expressed in Volt and the out voltage signal S produced by 1 e^- entering

377 in the preamplifier:

$$ENC = \frac{N_{out}[V]}{S_{out}[V/e-]} = \frac{V_{noise}^{RMS}}{G} \quad (3.1)$$

378 with G expressed in V/e-; as the gain increases, the noise reduces .

379 Considering the threshold dispersion a requirement for the ENC is:

$$ENC < \sqrt{(T/3.7)^2 - T_{RMS}^2(x) - T_{RMS}^2(t)} \quad (3.2)$$

380 where the T is the threshold set, T_{RMS} is the threshold variation during time (t) and
381 across the matrix (x); a typical reasonable value often chosen is 5 ENC.

382 Because of the changing of the 'real' threshold, the possibility of changing and adapting
383 the setting parameters of the FE, both in time and in space is desiderable: these parameters
384 are usually set by Digital to Analog Converter (DAC) with a number of bit in a typical
385 range of 3-7. Unfortunately DAC elements require a lot of space that may be not enough
386 on the pixel area; therefore, the FE parameters are typically global, which means that they
387 are assigned for the whole chip, or they can be assigned for regions the matrix is divided
388 into. The former case corresponds to TJ-Monopix1's design in which 7 bits are used for
389 a total 127-DAC possible values, while the latter corresponds to the ARCADIA-MD1's
390 one, **where quanti bit??**. An other possibility, for example implemented in TJ-Monopix2,
391 is allocate the space on each pixel for a subset of bits, then combinig the global threshold
392 with a fine tuning. If so, the threshold dispersion after tuning is expected to decrease
393 depening on the number of bits available for tuning:

$$\sigma_{THR,tuned} = \frac{\sigma_{THR}}{2^{nbit}} \quad (3.3)$$

394 where σ_{thr} is the RMS of the threshold spread before tuning.

395 To measure the threshold and noise of pixels a possible way is to make a scan with
396 different known injected charge: the threshold corresponds to the value where the efficiency
397 of the signal exceeds the 50%, and the ENC is determined from the slope at this point.
398 Assuming a gaussian noise, e.g. a noise whose transfer function turns a voltage δ pulse in a
399 gaussian distribution, the efficiency of detecting the signal and the noise can be described
400 with the function below:

$$f(x, \mu, \sigma) = \frac{1}{2} \left(1 + erf \left(\frac{x - \mu}{\sigma\sqrt{2}} \right) \right) \quad (3.4)$$

401 where erf is the error function. Referring to 3.4 the threshold and the ENC corresponds
402 to the μ and σ .

403 I used the injection circuit available on the chip to inject 100 pulses for each input
404 charge for a fixed threshold. The injection happens on a capacity at the input of the FE
405 circuit, whose nominal value is 230 aF and from which the conversion factor from DAC
406 units to electrons can be obtained: for the PMOS flavor, for example, since the DAC are
407 biased at 1.8 V, the Least significant Bit (LSB) corresponds to a voltage of 14.7 mV from
408 which the charge for LSB $1.43 \text{ e-}/\text{mV}$ and the conversion factor therefore is $20.3 \text{ e-}/\text{DAC}$.
409 While this value is equivalent for all the PMOS flavor, the HV flavor is expected to have a
410 different conversion factor, $\sim 33 \text{ e-}/\text{DAC}$, beacuse of the different input capacity. Besides
411 the charge, also the duration and the period of the injection pulse can be set; it is important
412 to make the duration short enough to have the falling edge during the dead time of the
413 pixel (in particular during the FREEZE signal) in order to avoid the undershoot, coming

	PMOS A	PMOS B	PMOS C	HV
Threshold [e ⁻]	401.70±0.15	400.78±0.24	539.66±0.58	403.87±0.19
Threshold dispersion [e ⁻]	32.90±0.11	32.97±0.17	55.54±0.42	44.67±0.15
Noise [e ⁻]	13.006±0.064	12.258±0.068	13.88±0.11	11.68±0.10
Noise dispersion [e ⁻]	1.608±0.044	1.504±0.046	1.906±0.072	1.580±0.068

Table 3.1: Mean threshold and noise parameters for all flavor and their dispersion on the matrix.

414 at high input charge, triggering the readout and reading spurious hits. Since the injection
 415 circuit is coupled in AC to the FE, if the falling edge of the pulse is sharp enough to
 416 produce an undershoot, this can be seen as a signal.

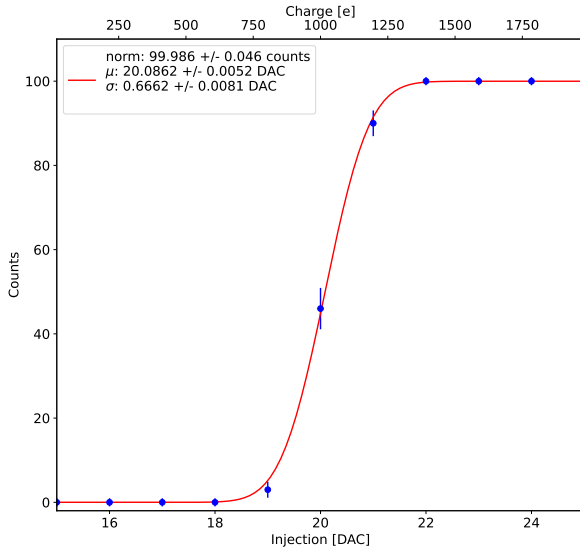


Figure 3.1: S-curve for pixel (10, 10) of the PMOS flavor (flavor B) with IDB fixed at 40 DAC. The conversion of charge injected from DAC to electrons has been performed using a nominal conversion factor of 20.3 e⁻/DAC *Mi sono resa conto che l'asse superiore è sbagliato. Devo rigenerare il plot*

417 with IDB equal to 40 DAC

418 Therefore I fitted the counts detected using the function in equation 3.4. Figure 3.1
 419 shows an example of such fit for a pixel belonging to the flavor B, while in figure 3.2 are
 420 shown the 1D and 2D distributions of the parameters found. I fitted the 1D distributions
 421 with a gaussian function to found the average and RMS of the noise and the threshold for
 422 each flavor across the matrix. The results are reported in table 3.1.

423 In the map at the top right panel of figure 3.2 (IDB=40 DAC) a slightly lower thresh-
 424 old is visible in the first biasing section (columns from 0 to 14); similar structures, but
 425 extended to the entire matrix, appear more evidently when using different IDB values.
 426 The systematic threshold variation across the biasing group has not a known motivation,
 427 but one could certainly be the transistor mismatch of the biasing DAC registers IDB
 428 and ICASN, which both adjust the effective threshold (I recall that ICASN regulate the

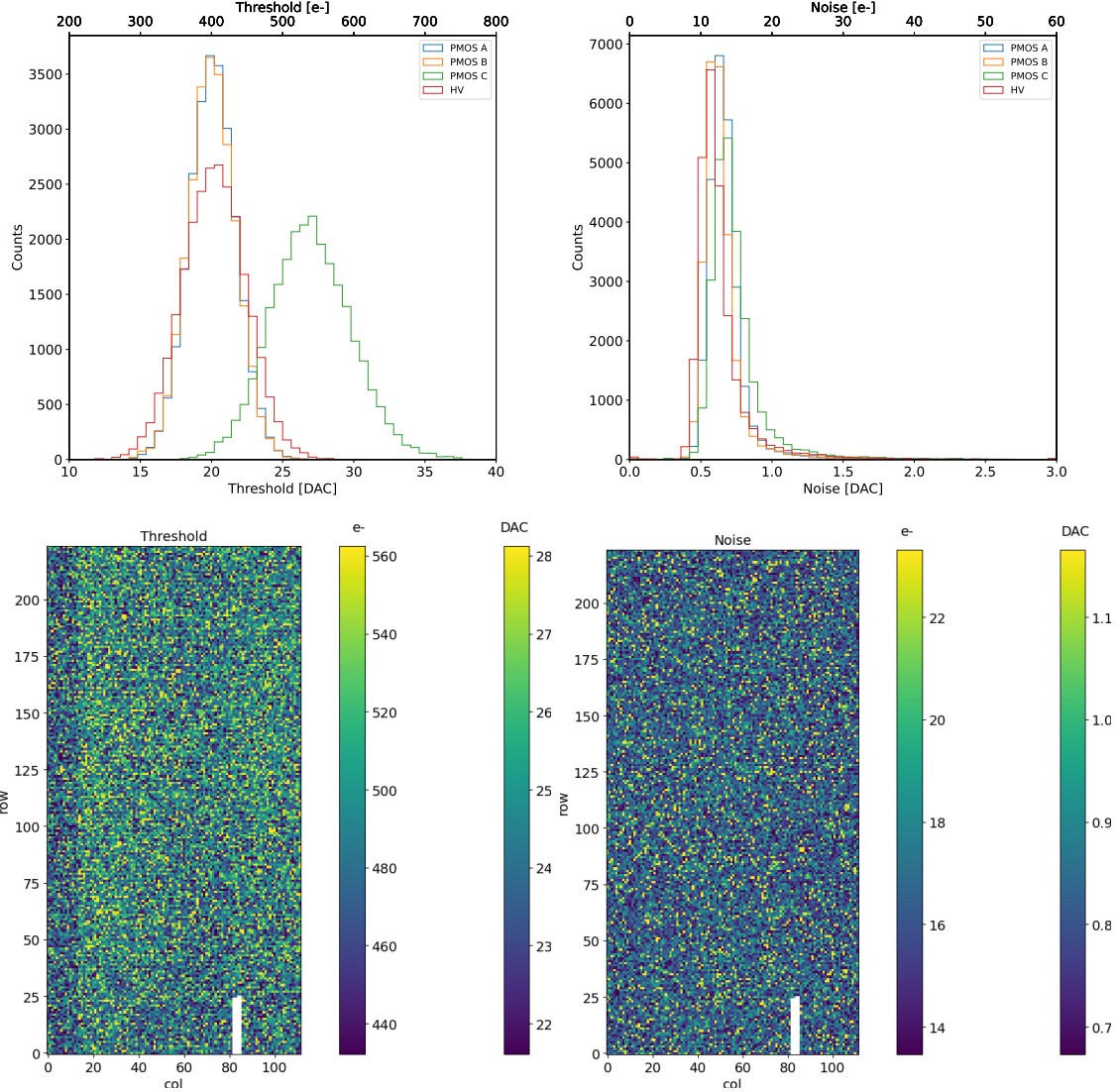


Figure 3.2: Histograms of the threshold (a) and the noise (b) found fitting the s-curve of all flavor with IDB fixed at 40 DAC. Below there are the maps of the threshold (a) and the noise (b), respectively, found fitting the s-curve with IDB fixed at 40 DAC for the PMOS flavor (B). The white pixels have the injection circuit broken.

429 baseline).

430 To verified the trend of the threshold as a function of the front end parameter IDB and
 431 find its dynamic range, I have permormed different scans changing the FE register IDB.
 432 For each IDB I have injected the whole matrix and search for the mean and the standard
 433 deviation of the threshold and noise distributions. The results are shown in figure 3.3:
 434 the blue points are the mean threhsold found whithin the matrix, while in green is shown
 435 the width of the threshold distribution, aka the threshold dispersion. While the threshold
 436 increases, the ENC decreases of $\sim 4 \text{ e-}$,which is $\sim 1/3$ of the noise at IDB=40 DAC.

437 Then, to evaluet the operation and the occupancy of the chip at different threshold
 438 I have made long acquisitions of noise at different IDB and check how the number of
 439 pixel masked changes with the threshold. The masking algorithm I have used search for
 440 pixels with rate $> 10 \text{ Hz}$ and mask them. With such algorithm, in our standard condition,

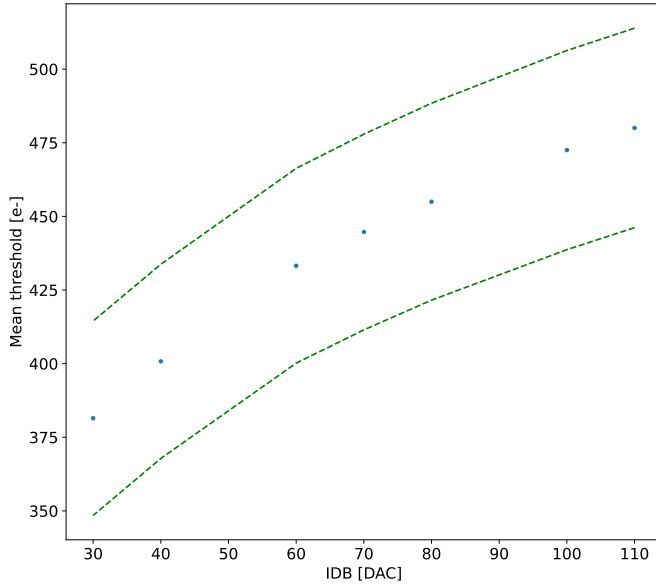


Figure 3.3: Flavor PMOS (B) with Psub-Pwell biased at -6 V. Threshold measured in electrons vs the register which sets the threshold, IDB.

441 IDB=40 DAC, a very low noise hit rate is intentionally achieved masking a dozen of pixels
 442 of the whole flavor.

443 3.1.2 Linearity of the ToT

444 I have already said in chapter 1 that TJ-Monopix1 returns an output signal proportional to
 445 the charge released by a particle in the epitaxial layer, which is the Time over Threshold;
 446 the ToT is saved as a 6-bit variable and then has a dynamic range equal to 0-64, which
 447 corresponds to 0 μ s to 1.6 μ s assuming a clock frequency of 40 MHz. When a pulse is longer
 448 than 1.6 μ s the counter rolls back to zero and there is no way to distinguish that charge
 449 from a lower one with the same ToT: that is the rollover of the ToT (3.4(a)).

450 In order to associate the ToT (in range 0-64) to the charge, a calibration of the signal
 451 is necessary. Assuming the linearity between ToT and the charge, Q can be found:

$$Q [DAC] = \frac{(ToT [au] - offset [au])}{slope [au/DAC]} \quad (3.5)$$

452 where m and q are the fitted parameters of the calibration. It is important to keep in mind
 453 that the main application target of TJ-Monopix1 is in the inner tracker detector of HEP
 454 experiments, then the main feature is the efficiency, then a rough calibration of the signal
 455 to charge is fine. The ToT information can be used both to better reconstruct the charge
 456 deposition in cluster in order to improve the track resolution, and for particle identification,
 457 especially for low momentum particles which do not reach the proper detectors.

458 The study of the output signal is made possible via the injection: since the pulses
 459 are triangular, the ToT is expected to be almost therefore, to prevent th linear. To verify
 460 this statement and study the deviations from linearity I fitted the ToT versus the charge
 461 injected for all the pixels within the matrix. In figure 3.4(b) there is an example of fit

462 for a pixel belonging to the flavor B, while in figure 3.5 there are the histograms and the
 463 maps of the parameters of the line-fit for all flavors with IDB fixed at 40 DAC. Here again
 464 a difference among the biasing section appears: since the slope of the ToT is related with
 465 the gain of the preamplifier (increasing the gain also increases the ToT), the mismatch is
 466 probably due to the transistor contributing to the amplification stage.

467 I fitted the average ToT of all the pulses recorded as a function of the pulse amplitude;
 468 data affected by rollover have been removed in order to avoid introducing a bias in the
 469 mean values. In figure 3.4 (b) are shown both the fits with a line (red) and with a second
 470 order polynomial (green): at the bounds of the ToT range values deviate from the line
 471 model. Since the deviation is lower than 1% and it only interests the region near the 0
 472 and the 64, in first approximation it is negligible.

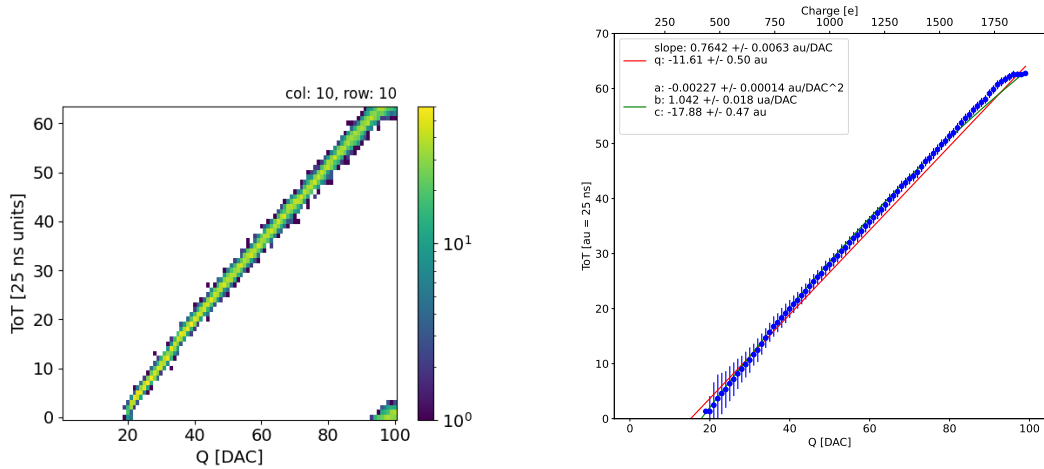


Figure 3.4: The figures refer to pixel (10,10) of the PMOS-reset flavor B with IDB fixed at 40 DAC. (a) Histogram of the injection pulses: the ToT is in range 0-64 since it is represented by 6 bit, so when achieving the 64 it rolls over back to the zero. (b) Mean ToT vs the the charge: the mean has been calculated cutted the rolling hits.

473 3.1.3 Calibration of the ToT

474 Finding a calibration for the ToT means defining a way to pass from the ToT values
 475 (0-64 clock counts) to a spectrum expressed in electrons collected. The principles of the
 476 calibration are the following: the ToT in clock counts maps (eq.3.1.2) a DAC range between
 477 the threshold and a value which depends on the pixel and generally is around 90-100 DAC.
 478 Assuming that a 0 DAC signal corresponds to 0 e⁻, if another reference point is fixed, a
 479 linear calibration function can be defined. After the calibration the ToT goes to map
 480 a charge range between the threshold and Q_{max} which is a function of the pixel and is
 481 around 2 ke⁻.

482 Moreover, considering that the charge injected in the FE goes to fill a capacitor C
 483 which is different from pixel to pixel, the true charge injected does not correspond to what
 484 expected assuming C equal to 230 aF, which is the nominal value. Accordingly to that,
 485 a measurement of this value provides both an absolute calibration of C and a conversion
 486 factor K to have a correspondence of the DAC signal in electrons. K and C are defined

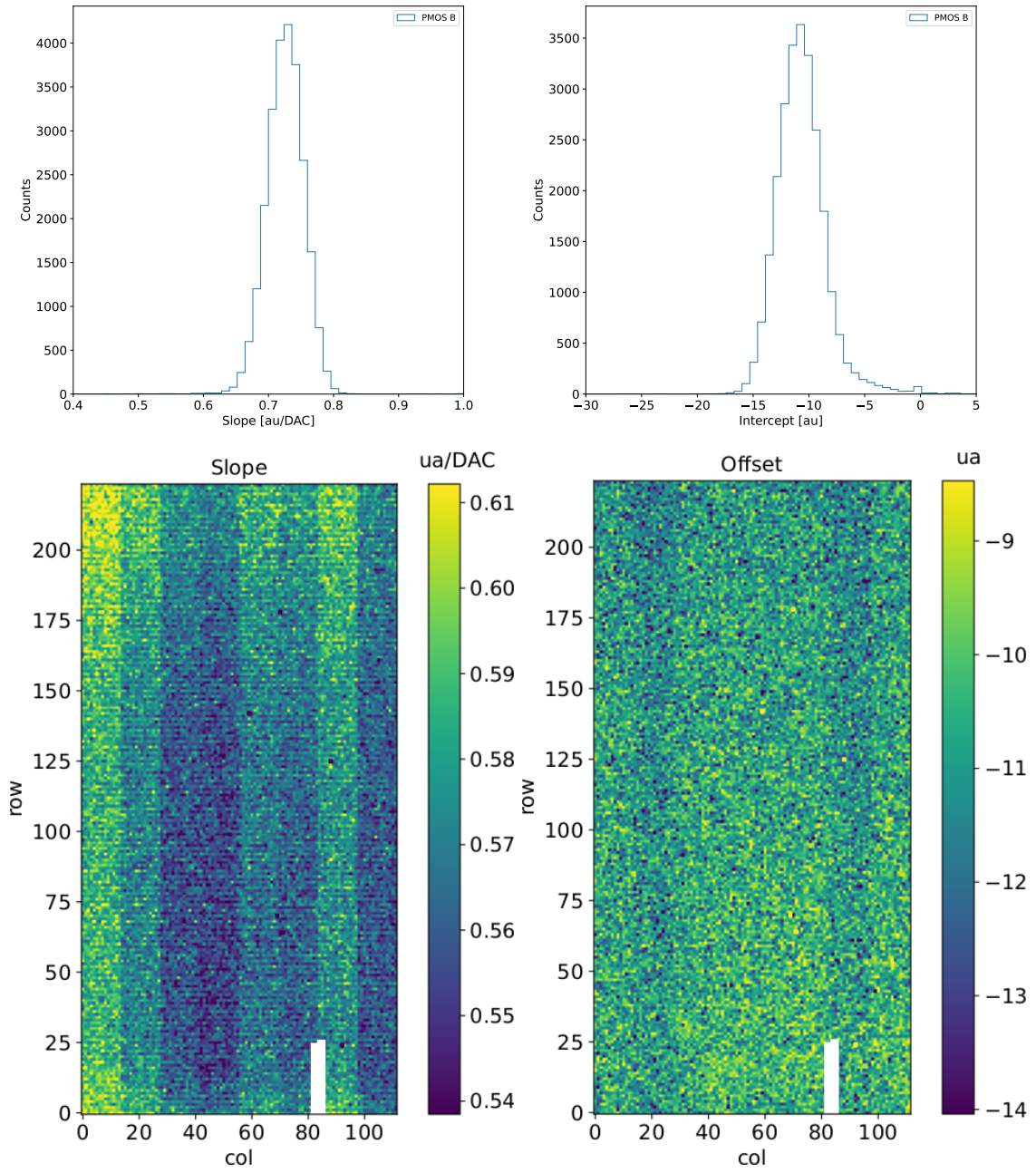


Figure 3.5: Histograms of the calibration parameters, slope (a) and offset (b), found fitting the ToT with a line, for the flavor B and with IDB fixed at 40 DAC. Maps of the calibration parameters, slope (a) and offset (b), found fitting the ToT with a line, with IDB fixed at 40 DAC.

487 respectively as:

$$K [e^- / DAC] = \frac{1616 [e^-]}{Q [DAC]} \quad (3.6)$$

488

$$C [F] = [e^- / DAC] \frac{1.6 \cdot 10^{-19} [C]}{14.7 [mV]} \quad (3.7)$$

489 where K is expected to be $20 e^- / DAC$, assuming the nominal value of C equal to $230 aF$,
490 and where 1616 is the expected number of electrons produced by the calibration source

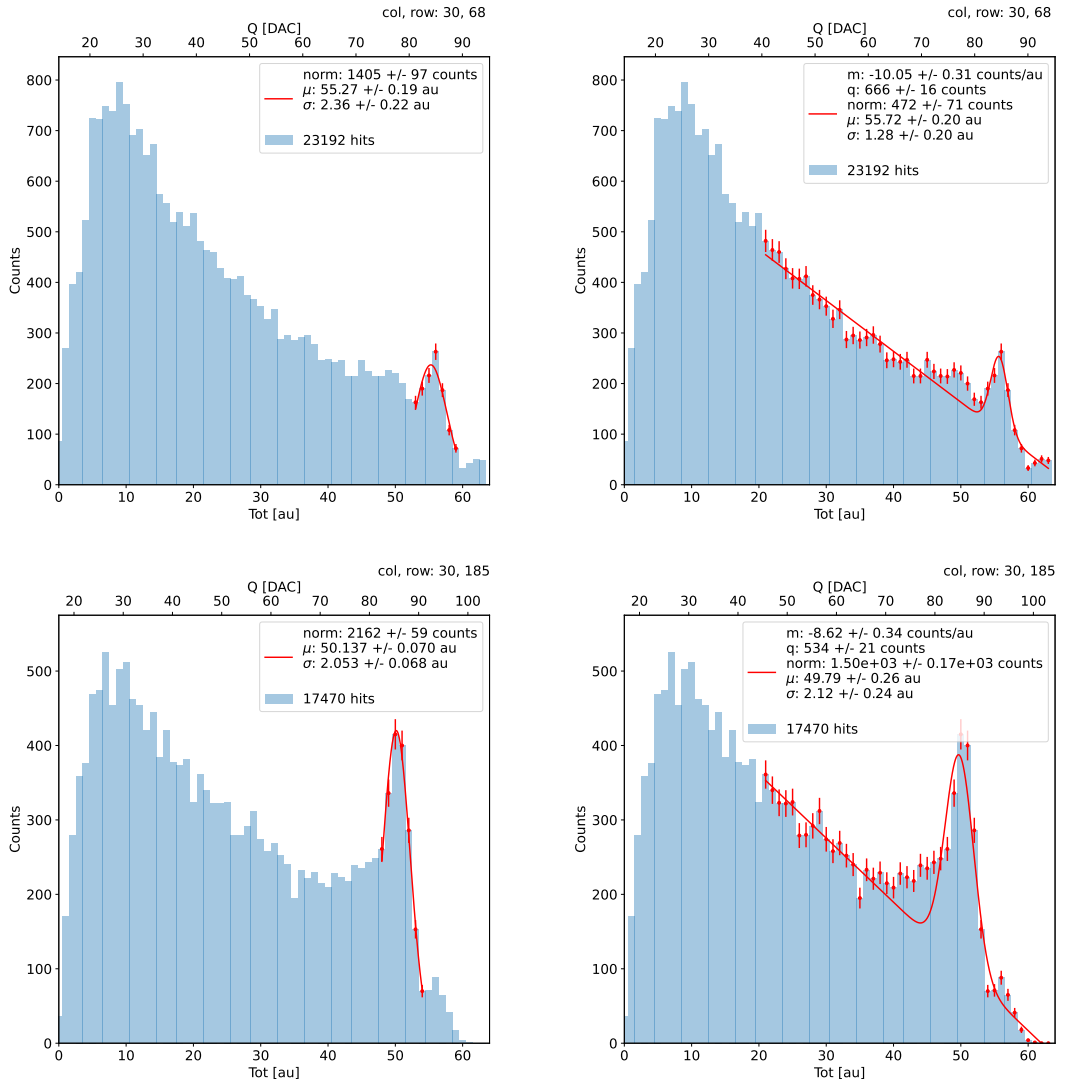


Figure 3.6: due pixel per far vedere la differenza tra i fit. Sottolinea che in rosso ci sono i bin fittati. La doppia scala utilizza le info trovate nel paragrafo precedente per il dato pixel in questione. Per avere una corrispondenza grezza in elettroni basta moltiplicare per 20 e- / dac.

used, Fe55. Fe55 is an extremely important radionuclide in the calibration of X-ray spectrometers, proportional counter and scintillator detector since it emits two X-photons during the electron capture decay: the first one (K_{α}) at 5.9 keV and the second one (K_{β}) at 6.5 keV. The K_{α} photon, which does photoelectric effect in silicon, has an absorption length $\lambda=7 \mu\text{m}$ to $8 \mu\text{m}$, and the probability of being absorbed in the $25 \mu\text{m}$ thick epitaxial layer is $\sim 0.95\%$. The electron emitted has an energy equal to the photon, so recalling that the mean energy needed to produce a couple electron-vacuum is 3.65 eV, the signal produced by the Fe55 source is expected to be 1616 e^- . In figures 3.6 are shown two histograms of the ToT spectrum of the Fe55 source for two different pixels. The peak on the right corresponds to the events with complete absorption of the charge in the depleted region, while the long tail on the left to all the events with partial absorption due to charge sharing among neighbors pixels. In order to reduce the consistent charge sharing, the pixel dimension in TJ-Monopix2 has been reduced down to $30 \times 30 \mu\text{m}^2$. The events on the right

504 side of the peak, instead, corresponds to the K_β photons. Looking at the histograms for
 505 pixel (30, 185) and (30, 69) a significant difference in the peak to tail ratio leaps out, which
 506 can be related with the position of the pixel in the matrix. In particular, because of a
 507 different charge collection property, pixels in the upper part of the matrix (rows 112-224)
 508 have a more prominent peak, while in pixels in the lower part (rows 0-111) there is a
 509 higher partial absorption. Indeed, as discussed in section ??, there is a distinction in the
 510 structure of the low dose-epi layer among the rows, in particular pixels in rows 112-224,
 511 which have a RDPW, are supposed to have a higher efficiency in the pixel corner.

512 For the calibration I needed to establish the peak position; to do that I fitted the ToT
 513 histogram of each pixel. I tested two different fit functions:

$$f(x, N, \mu, \sigma) = \frac{N}{\sigma\sqrt{2\pi}} e^{-\frac{1}{2}(\frac{(x-\mu)}{\sigma})^2} \quad (3.8)$$

514

$$f(x, m, q, N, \mu, \sigma) = m x + q + \frac{N}{\sigma\sqrt{2\pi}} e^{-\frac{1}{2}(\frac{(x-\mu)}{\sigma})^2} \quad (3.9)$$

The additional linear term in equation 3.9 is meant to model the tail due to incomplete

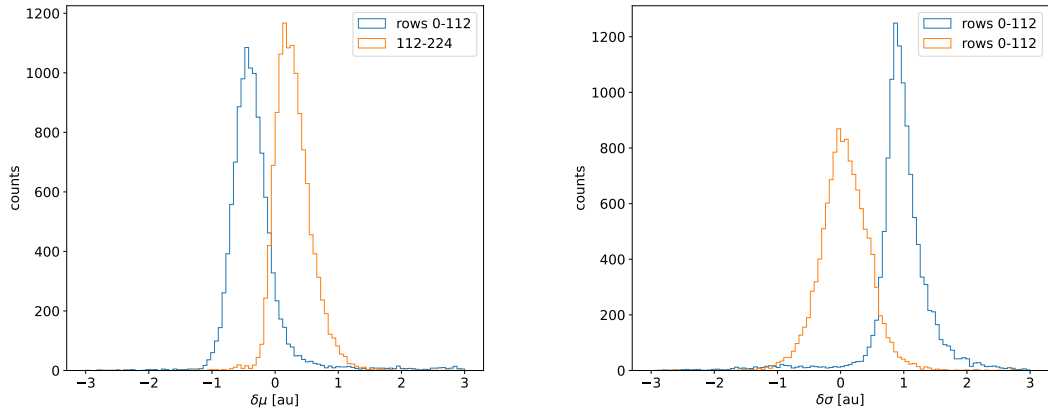


Figure 3.7: Difference between the parameters μ and σ obtained with the gaussian fit and those obtained with a gaussian plus a line. When $\mu < 0$ the fit with function 3.8 is generally worse (the peak is shifted to the left); when $\sigma < 0$, the fit with 3.9 is worse (larger sigma).

515

516 charge collection and prevent it from introducing a bias in the fitted peak position.

517 For this reason, when fitting with eq.3.9, I selected a larger region compared to the
 518 fit with eq.3.8, for which I used only a small reagion around the peak. The optimal fit
 519 region was chosen in both cases through an iterative routine: for the fit with eq.3.9 it
 520 starts from an interval including all the pixels above 20 DAC and progressively reduces it
 521 by increasing the left boundary; for the fit with eq.3.8, it starts from an interval of 5 bins
 522 around the expected peak position and reduces the interval of 1 bin at each iteration.

523 Even if the difference in the peak position between the two fit strategies is not really
 524 relevant for the purpose of the calibration, being of the order of 0.8-1.5% (3.7),it still
 525 introduces a systematic bias towards lower values due to the contribution of the tail.
 526 Indeed, we know that the sharp edge on the right must correspond to the case of complete
 527 absorption of the photon, so that, in general, the closest to this feature is the fitted peak
 528 position, the better the fit is. A poor fit tends also to overestimate the peak width. Even

529 looking at the χ^2 , the fit function 3.8 seems to be the better choice, except for a sample
 530 of pixels in the lower part of the matrix, the one with lower efficiency.

531 The resolution of the detector, which is expected to be determined by the statistical
 532 fluctuations in the number of charge carriers generated in the detector as well as by the
 533 ENC, can be compared to the observed Fe55 peak width. Ideally:

$$\sigma_{Fe} = \sqrt{ENC^2 + F \times N} \quad (3.10)$$

534 Since the number of e/h pairs produced in the sensor is 1616, recalling that F for a silicon
 535 detector is 0.115 and that the ENC measured with the injection is 12e- , the σ_{Fe} is
 536 expected to be $\sim 18\text{e-}$. Looking at figure 3.8 the resolution achieved with the Fe55 source
 537 seems to be much higher. A contribution we have not taken into account but is certainly
 538 relevant is the systematic overestimation of the standard deviation of the Fe55 peak: this,
 539 as I already explained, is principally due to the high background of incomplete charge
 540 collection, which broadens the fitted peak.

541 2D maps of the value of the capacity and of the conversion factor found are shown in
 542 3.9. The evident stripe-structure in the matrix shows an evident correlation among the
 543 same row; the same structure, which is also visible in the slope map of the calibration of
 the ToT (fig.2.3), may be related with the structure of the bias lines.

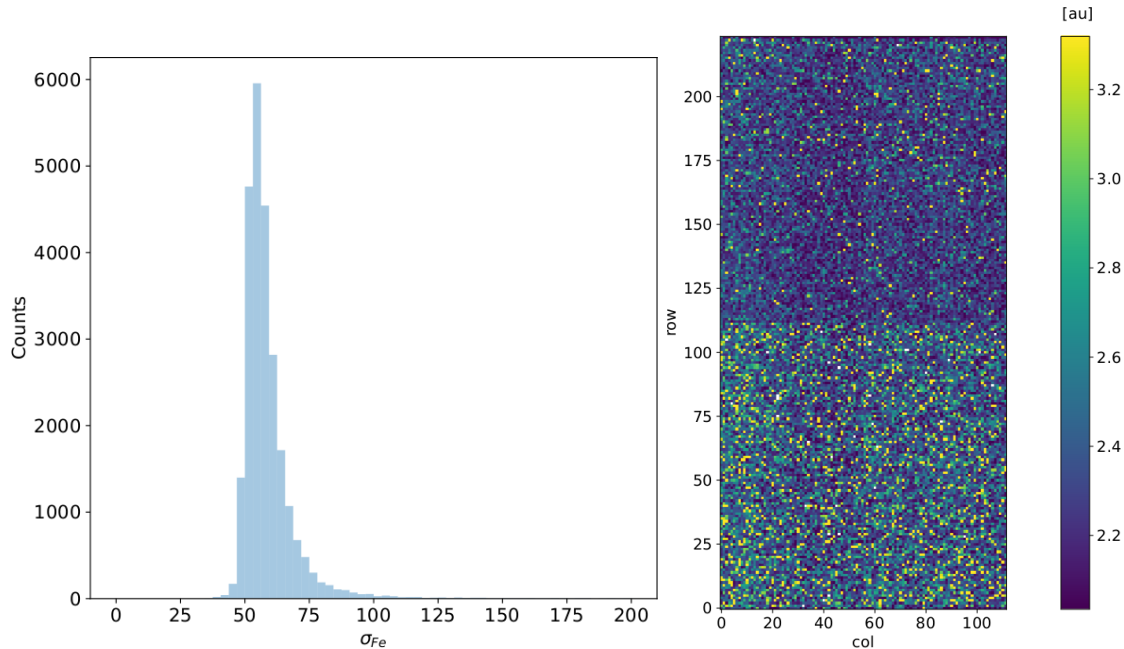


Figure 3.8: Histogram (a) and map (b) of the fitted Fe55 peak width.

544

545 HV flavor calibration

546 An attempt of calibrating the HV flavor, which is the most different from the PMOS B
 547 flavor, has been performed; however, because of the loss of signal caused by the higher
 548 capacity, we have been unable to identify the Fe55 peak in every FE and bias configuration.
 549 An example of Fe55 spectrum collected with the HV flavor is shown in figure 3.10.

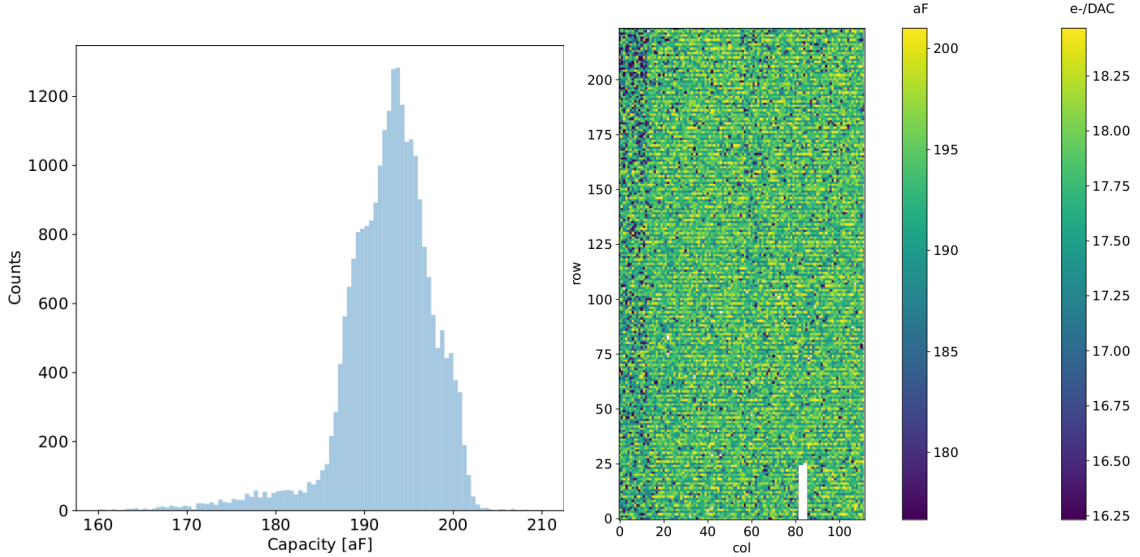


Figure 3.9: Histogram (a) and map (b) of the calibrated capacity of the injection circuit.

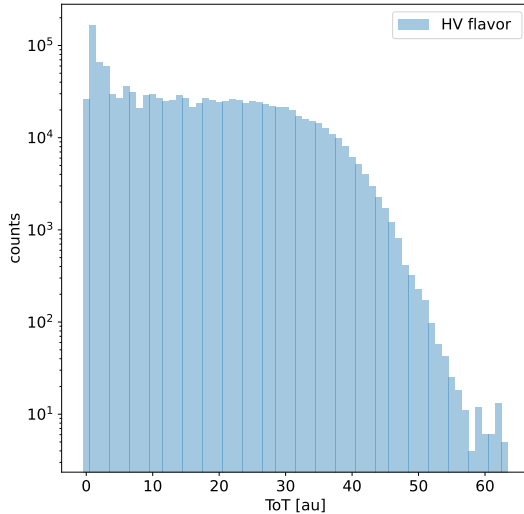


Figure 3.10: Fe55 spectrum with the HV flavor

550 3.1.4 Changing the bias

551 In order to study the behavior of the sensor as a function of the bias, I performed several
 552 injection scans in different configurations. Indeed, the thickness of the depletion region has
 553 to be considered an important parameters affecting the signal efficiency, and in particular
 554 it affects the charge released by a particle which crosses the sensor (since the signal is
 555 proportional to the thickness of the epitaxial layer). The measured output voltage ampli-
 556 tude and gain in the case of the PMOS and HV flavours are shown in figure 3.11 Given
 557 that the chip under examination has a gap in the low dose epi-layer, we were not able to
 558 change independently the bias of the substrate (PSUB) and of the p-well (PWELL), but
 559 they must be kept at the same value, differently from other chips of the same submission.
 560 Lowering the bias, the depletion region is expected to narrow and the efficiency to reduce,

	-6 V	-3 V	0 V
Threshold [DAC]	20.0 ± 1.6	21.0 ± 1.6	24.5 ± 1.8
Noise [DAC]	0.613 ± 0.075	0.625 ± 0.078	0.822 ± 0.098
Slope [au/DAC]	0.726 ± 0.027	0.707 ± 0.028	0.573 ± 0.021
Offset [au]	-10.8 ± 1.9	-11.2 ± 1.8	-11.1 ± 1.5

Table 3.2: The errors are the standard deviations of the corresponding distributions. The conversion factor from DAC to electrons is $\sim 20 \text{ e}^-/\text{DAC}$.

especially in the pixel corner, thus raising the threshold and the noise and decreasing the slope as a consequence of the reduction in the gain.

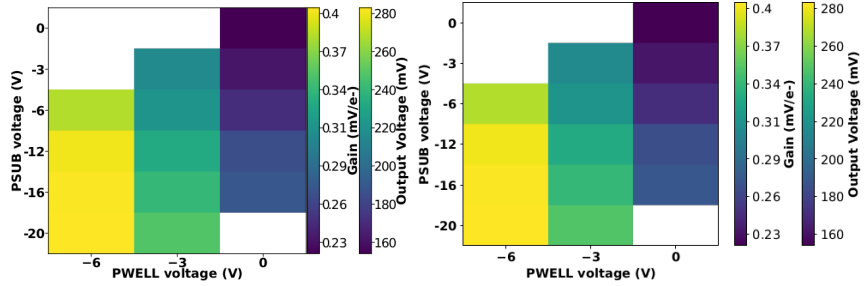


Figure 3.11: Output voltage amplitude and gain with respect to the p-well and p-substrate voltage in the case of the PMOS reset front-end (B)

In order to test the behavior of the chip when not completely depleted, I have performed an injection scan with PSUB/PWELL bias at 0 V, -3 V and -6 V (results in tab.3.2), and some acquisitions with the Fe55 source (fig. 3.12). There are reported the values of the K_α peak position, the normalization of the events above the peak and the rate, everything has been normalized to the value at the reference condition, which is with PSUB/PWELL at -6 V.

3.1.5 Measurements with radioactive sources

In order to completely validate the operation of the whole sensor¹, I have performed several acquisitions with radioactive sources, specifically Fe55 and Sr90Y, which is a β^- emittitor with electron endpoint at 2.2 MeV, and cosmic rays. I used the data collected with Sr90 and cosmic rays, to study charge sharing and events with more than one hit.

I define *cluster* the ensamble of all the hits with the same timestamp. This is obviously a coarse requirement, but it gave me the opportunity of using a simple and fast clustering algorithm, which is fine when the random coincidence probability is neglibile. Defining R_1 and R_2 as the two events rate, and τ as the dead time of the detector, the random coincidence rate can be found:

$$R_{coinc} = R_1 \times R_2 \times \tau \quad (3.11)$$

As I am going to prove in the next section, the dead time strictly depends on the occupancy of the matrix, even though we can assume a dead time of $\sim 1 \mu\text{m}$, which corresponds to

¹As I will discuss in chapter 4.2 these measurements serves also as a reference for the spectrum observed at the test beam

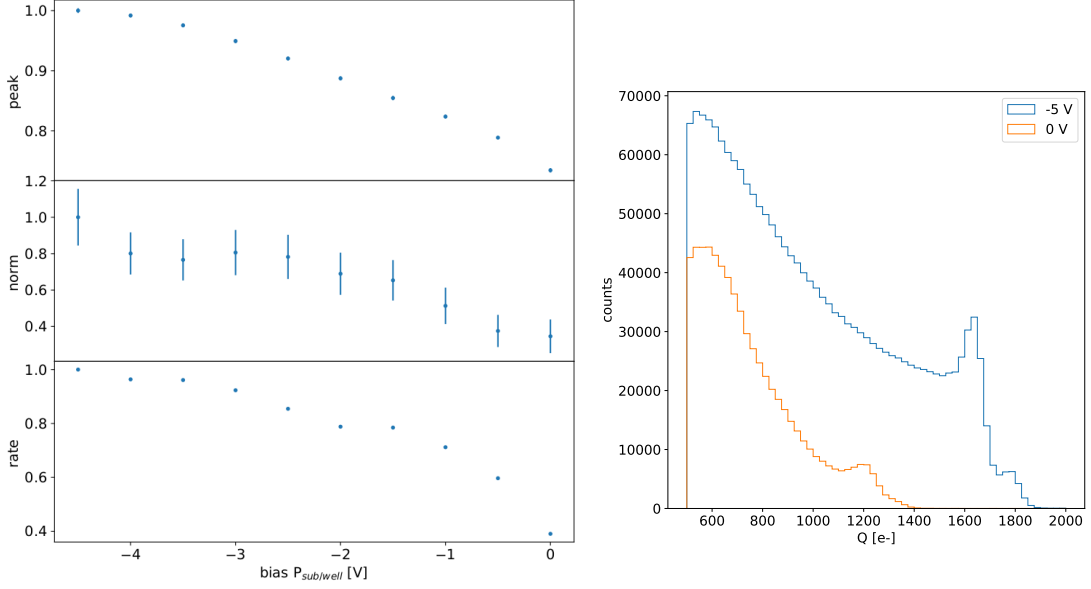


Figure 3.12: (a) Peak position, peak amplitude and rate as a function of the bias. Since during the collection of the whole data the source has been moved, it is not guaranteed that it has always had a repositioning in the same exactly place, then small the fluctuation of the rate along the decreasing trend are acceptable. The peak position and amplitude are estimated by fitting the spectrum with a gaussian in the region around the peak. (b) Fe55 spectrum at different $P_{sub/well}$ bias. The ToT values have been calibrated as explained in section. 3.1.3.

581 the mean dead time per pixel. However, if in an event a particle hits two different pixels
 582 producing a cluster, the total dead time simply doubles. Since the measured rate on the
 583 whole matrix of noise, Fe55, Sr90 and cosmic rays are \sim Hz, 3.3 kHz, 40 Hz and \sim 10 mHz²,
 584 the random coincidence probability are negligible except the one of two Fe55 events, which
 585 is 11 Hz.

586 In figure 3.13 I report the histograms of the number of pixels in the cluster and of the
 587 dimension of clusters, defined in terms of the max and min coordinates on the matrix as:

$$d = \sqrt{(y_{max} - y_{min})^2 + (x_{max} - x_{min})^2} \quad (3.12)$$

588 Looking at the shape of the histogram of the dimension, generally the Sr90 and the
 589 cosmic rays produce bigger clusters and hit a higher number of pixels, a trend that can
 590 be explained considering that the Fe55 photoelectron is much less energetic than the Sr90
 591 electron and cosmic rays. Below I have also attached a sample of hitmap of events produced
 592 by the three different sources (fig.3.14, 3.15).

593 In figures 3.18, 3.19, 3.21 are shown the distributions per different cluster dimension
 594 events, of the charge collected by a single pixel (figures on the left) and the charge collected
 595 by summing the charge collected by the pixels within the cluster (figures on the right).
 596 Since the noise rate is comparable with the cosmic rays and Sr90 ones, I have removed the
 597 single pixel events which are separately shown in figure 3.17; despite we cannot identify
 598 and selecting only the noise events, these distributions, and especially the cosmic rays
 599 one, are expected to be mostly populated by noise events. The distributions have a peak

²The cosmic rays rate at the sea level is expected to be \sim 1/cm²/s

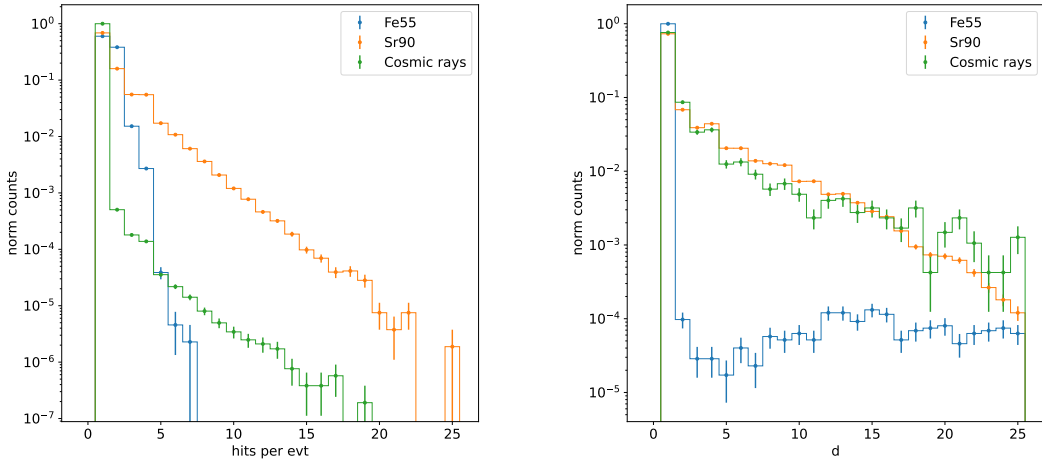


Figure 3.13: (a) Distribution of the number of hits per event with different sources. (b) Dimension of cluster defined as eq.3.1.5. Compared with the Sr90 and the cosmic rays, the Fe55 d distribution is characterized by a clear discontinuity in the cluster dimension. The very thin peak around 0 corresponds to the effective cluster, while the long tail at bigger cluster d is principally made of random coincidence.

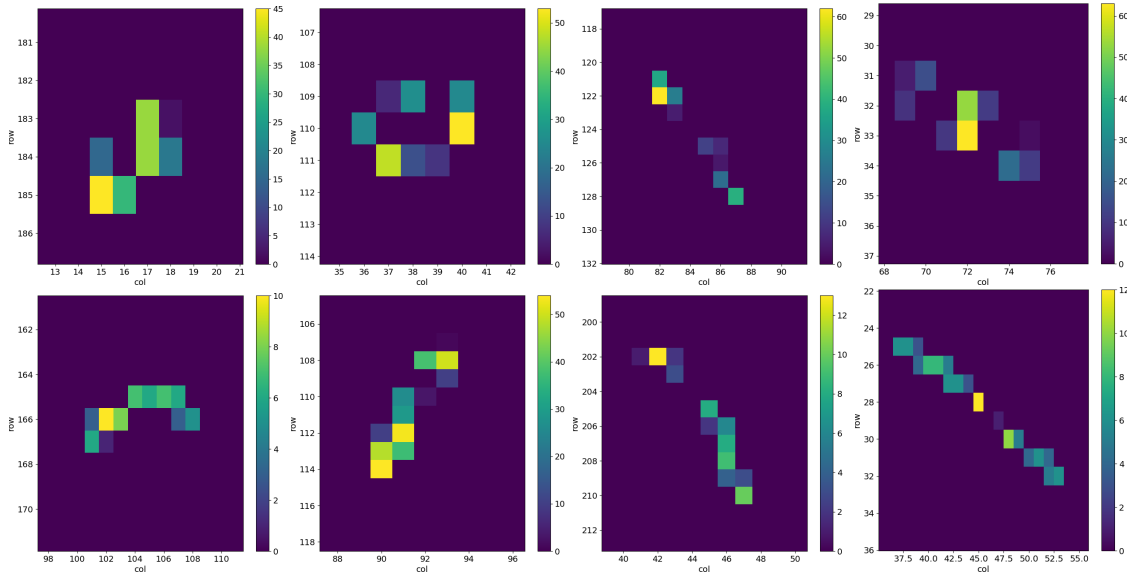


Figure 3.14: 2D histograms of the ToT in different events in an acquisition of cosmic rays.

around the threshold, which is compatible with the fact that the noise events typically have a low ToT.

Looking at the spectra of Sr90 instead (fig:3.19), the maximum of the distribution of the cluster charge seems to follow a linear dependence on the number of pixels hit (tab.3.3); this can be accepted as a first approximation considering that the pitch ($36\text{ }\mu\text{m}$ and $40\text{ }\mu\text{m}$) depending on the direction, and the epitaxial layer thickness ($25\text{-}30\text{ }\mu\text{m}$) are comparable. However a more accurate model which takes into account the impact angle of the particle should be developed for a more precise comparison. The charge per length covered Q/l released by a particle which crosses more pixels and is not completely absorbed in the

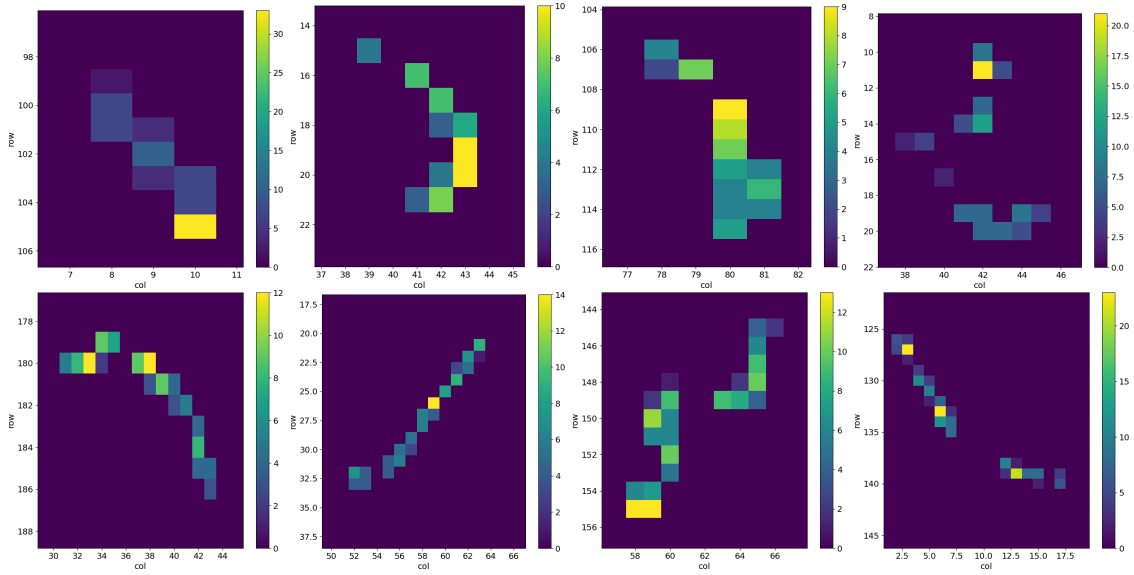


Figure 3.15: 2D histograms of the ToT in different events in an aquisition of Sr90.

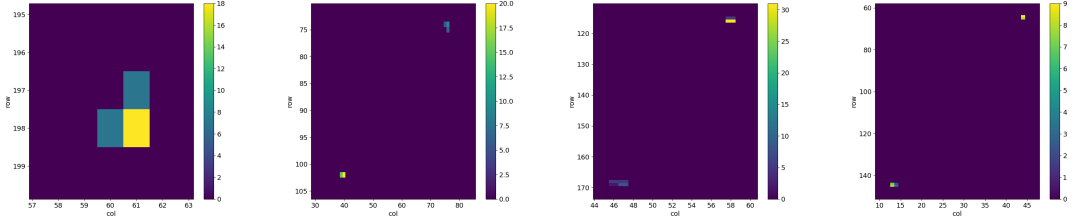


Figure 3.16: 2D histograms of the ToT in different events in an aquisition of Fe55

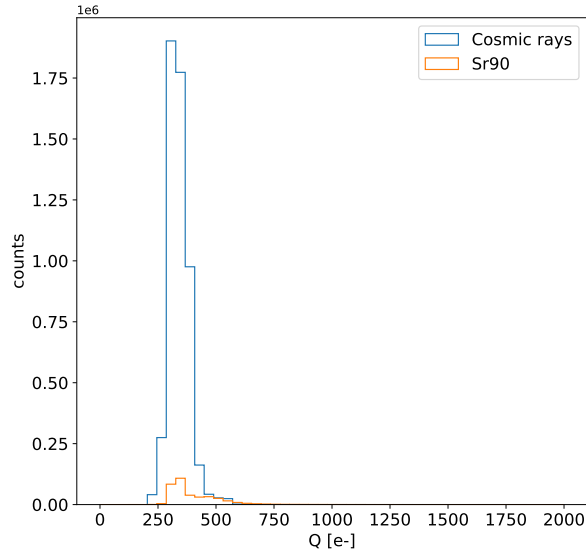


Figure 3.17: Histograms of the charge released in the pixels in events in which only a single pixel turns on.

Pixel per evt	Measured [e-]
2	950 ± 30
3	1450 ± 30
4	2050 ± 30
5	2450 ± 30

Table 3.3: Position of the maximum of the distributions in figure 3.19(b) of the summed charge released in the clusters depending on the number of pixel in the cluster.

609 sensor (fig.??) can be described by the following relation. Considering that:

$$l = \frac{t}{\cos(\lambda)} = \frac{t}{\sqrt{1 + tg^2\lambda}} = \frac{t}{\sqrt{1 + (x/t)^2}} \quad (3.13)$$

610 it can be expressed as:

$$\frac{Q}{l} = \frac{Q}{t} \sqrt{1 + (n - 1)^2 p^2 / t^2} \quad (3.14)$$

611 where p/t is the ratio between the pitch and the epitaxial layer thickness, and then it
 612 is different in the x and y directions ($40 \mu\text{m}$ and $36 \mu\text{m}$ respectively). Taking as value of
 613 p/t 1.52, which is the mean on the two axis, the value of Q/l expected by the scaling
 614 relation and the charge actually measured in the acquisition with the Sr90 are illustrated
 615 in table 3.3; because of the decision of cutting the single pixel events in order to have
 616 a clean sample, the expected value has been obtained by the two hits cluster dividing
 617 the charge by 2. By the inversion of the formula ??, the single pixel charge is then
 618 expected to be 522 e-. FORSE DATO CHE LA MASSIMA CARICA RILASCIATA
 619 SCALA LINEARMENTE CON IL NUMERO DI PIXEL NON SCRIVEREI QUESTA
 620 COSA? O MAGARI LA METTO COME CORREZIONE? The measured value has been
 621 obtained by the maximum of the distributions in the left plots in ??

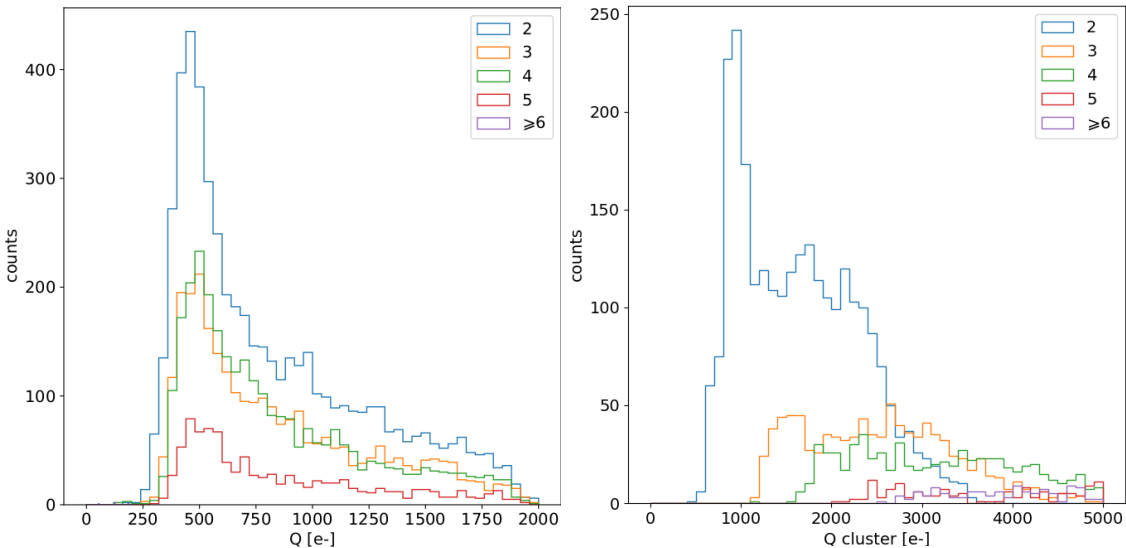


Figure 3.18: Acquisition of cosmic rays with IDB=40 DAC

622 Regarding the Fe55, the bump in the cluster spectrum at $\sim 1616 \text{ e-}$ corresponds to
 623 photons which had converted at the boundary of nearby pixels thus sharing their charge
 624 among them. Starting from 4-pixels clusters the peak moves to the right: this is due to

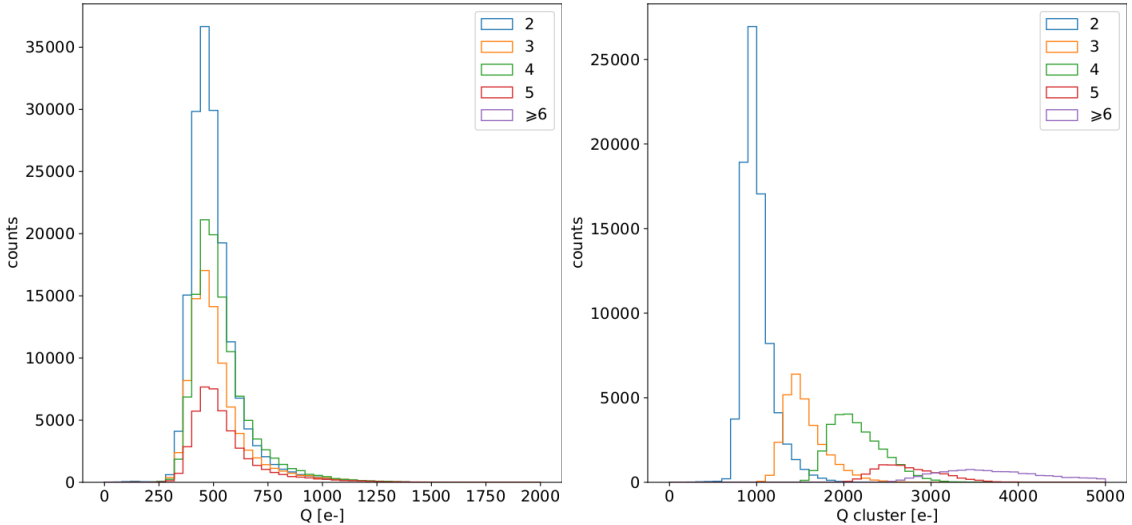


Figure 3.19: Acquisition of Sr90 with IDB=40 DAC

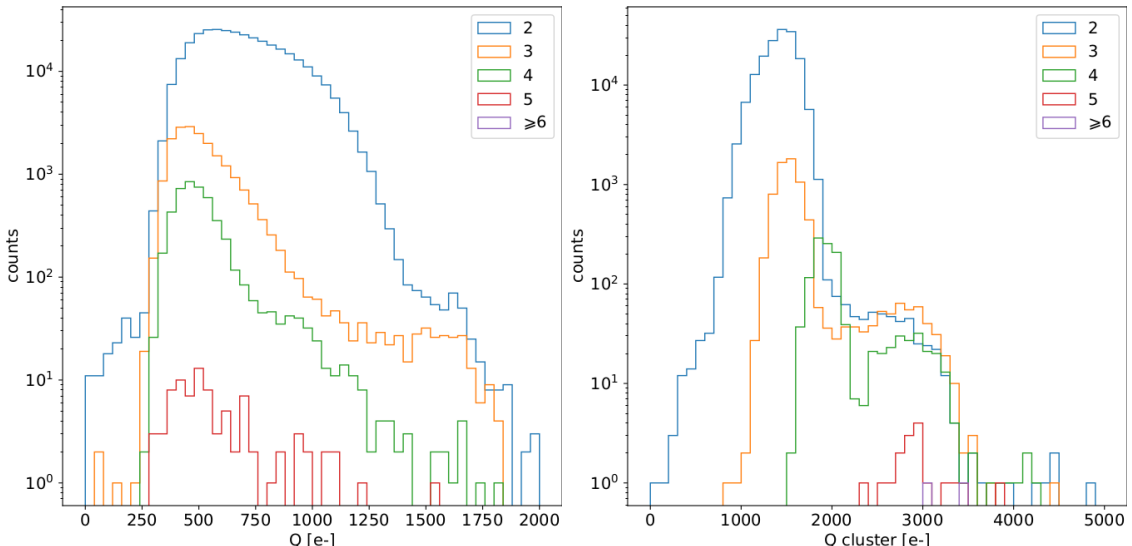


Figure 3.20: Acquisitions with radioactive source and cosmic rays at IDB=40 DAC.

Figure 3.21: Acquisition of Fe55 with IDB=40 DAC

the fact that the cluster with more than 3 pixels are principally random coincidence events Fe55-Fe55 or Fe55-noise. Recalling that the noise typically just exceeds the threshold and then has low ToT, the peak position in the spectrum 2.3 of 4-pixel cluster can be explained admitting that one of the four pixel is a noise signal. The shoulder on the right, instead, which have an edge at about 3200 e⁻ corresponds to the events with coincidence of two photons. Looking at the charge on the single pixel spectrum (fig.2.3), instead, a small bump can be seen around 1616 e⁻: these events correspond to photons which released almost all the charge on one pixel.

3.1.6 Dead time measurements

The hit loss is due to analog and digital pile up: the first one occurs when a new hit arrives during the pre-amplifier response, the second instead when the hit arrives while

636 the information of the previous hit has not yet been transferred to the periphery. Since the
 637 pre-amplifier response has a characteristic time \sim ToT, the dead time τ_a introduced by it
 638 will be at most 1.6 μ s; using the IRESET and VRESET FE parameters the reset time can
 639 be lowered down, but as explained in section ?? it must be longer than the preamplifier
 640 characteristics time in order to not cut the signal. Regarding the latter contribution instead,
 641 since only one hit at a time can be stored on the pixel's RAM, until the data have completed
 642 the path to get out, the pixel is paralyzed. Moreover since there is no storage memory
 643 included on TJ-Monopix1 prototypes, the digital dead time τ_d almost corresponds to the
 644 time needed to trasmit the data-packets off-chip.

645 The exportation of data from pixel to the EoC occurs via a 21-bits data bus, therefore
 646 only one clock cycle is needed and the dead time bottleneck is rather given by the
 647 bandwidth of the serializer which trasmits data off-chip from the EoC. In our setup the
 648 serializer operates at 40 MHz, thus to transmit a data packet (27-bit considering the ad-
 649 dition of 6 bits to identify the double-column at the EoC) at least 675 ns are needed. For
 650 what we have said so far, the R/O is completely sequential and therefore is expected a
 651 linear dependence of the reading time on the number of pixels to read:

$$\tau = 25 \text{ ns} \times (\alpha N + \beta) \quad (3.15)$$

652 where α and β are parameters dependent on the readout chain setting.

653 To test the linearity of the reading time with the number of pixels firing and to measure
 654 it, I have used the injection circuit which allows me choosing a specific hit rate: I made
 655 a scan injecting a fix number of pulses and each time changing the number of pixels
 656 injected. Indeed the injection mode allows fixing not only the amplitude of the pulse,
 657 which corresponds to the charge in DAC units, but also the time between two consecutive
 658 pulses (DELAY). The hit rate then corresponds to 25 ns/DELAY.

659 Unfortunately a high random hit rate on the matrix cannot be simulated by the in-
 660 jection because of the long time (\sim ms) needed to set the pixel registers of the injection;
 661 then I was forced to specify at the start of the acquisition the pixels to inject on, and for
 662 convenience I chose those on a same column. In figure 3.22 is shown the dependence of
 663 the efficiency on the DELAY parameter in two different cases. For the 5 pixels example
 664 the efficiency goes down the 90% at a DELAY of \sim 185 clock counts, which corresponds
 665 to 4.625 μ s and to a rate of 216 kHz, while in the 10 pixels example, the efficiency goes
 666 under the 100% at \sim 380 clock counts, which corresponds to 9.5 μ s and to a rate of 105 kHz.
 667 From the efficiency curves I have then looked for the time when the efficency decreases.
 668 In figure 3.23(a) is shown the dead time per pixels as a function of N with different R/O
 669 parameters configuration, the meaning of which is explained in chapter 1.3. The default
 670 value suggested by the designer of the chip are reported in table 3.4; moving too much
 671 the readout parameters from the default ones, the readout does not work properly, and no
 672 hits can be read at all. The problem probably stays in the firmware setting of the readout
 673 which are specially fixed for our chip **Sul repository, nei commenti ci sono altri valori pos-
 674 sibili per il FREEZE, ma avevamo detto che probabilmente sono relativi ai setting di altri
 675 chip.** Despite the single pixel reading time does not depend on the position on the pixel
 676 matrix, whithin a clock count which is \sim 25 ns, and it is equal to 106 clock counts, since
 677 the τ_d critically depends on the pixel position on the matrix: in particular the reading
 678 sequence goes from row 224 to row 0, and from column 0 to column 112, making the pixel
 679 on the bottom right corner the one with the longest dead time.

680 Furthermore to test that there is no dependece of the digital readout time from the

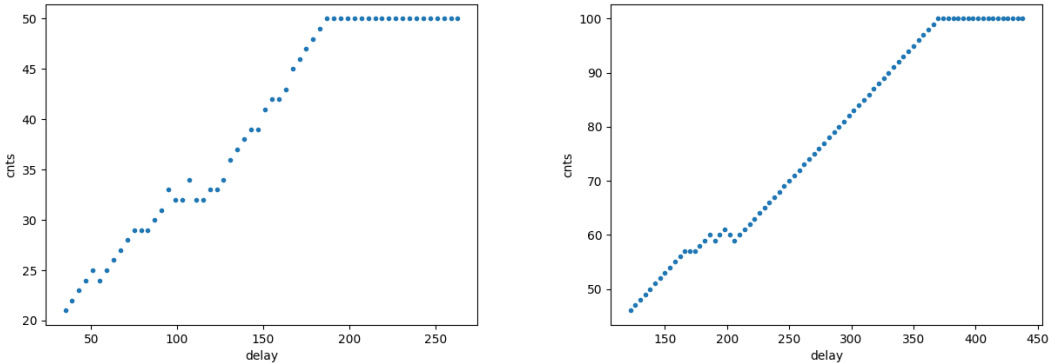


Figure 3.22: Efficiency vs the DELAY parameters. (a) I made a scan injecting 5 pixels with 50 pulses for each DELAY configuration and (b) 10 pixels with 100 pulses for each DELAY

Parameter	Value [DAC]	Value [μ s]
START_FREEZE	64	1.6
STOP_FREEZE	100	2.5
START_READ	66	1.65
STOP_READ	68	1.7

Table 3.4: Default configuration of the R/O parameters

charge of the pulse, I have try to change the amplitude of the pulse injected, but the parameters found were consistent with the default configuration ones. No difference in the α and β coefficients has been observed between the two case. Referring to eq.3.15, the factor α is proportional to the difference (STOP_FREEZE - START_READ), while the offset β lies between 5 and 15 clock counts.

The readout time found by this test is so long because in the prototypes no parallelization of the informations (with the instruction of more serializer for example) and no storage memory are included; this feature are typically added in the final prototypes. An example closely linked to TJ-Monopix1 is OBELIX: it will include on the chip a storage buffer to optimize the dead time and to keep a low occupancy even at high fluence.

3.2 ARCADIA-MD1 characterization

Unfortunatly the characterization of MD1 has not yet been completed because of some problems with the functionality of the first chip we received on which we have been able to make only a few electrical and communication test in order to test the operations of the FPGA and the breakount board (BB). We asked for another chip then but we, due to delay in the extraction and the bonding of the wafer, have received it one week ago; an exhaustive characterization and testing of the new chip have been going on in the clean room on the INFN, and I am going to show here only some preliminary results.

The problem with the broken chip occurs when it is biased, in particular, when the HV voltage is lowered down 0V, the sensor requires too much power and a too high current draw sets. We have discussed the problem with the designers of the chip whose helped

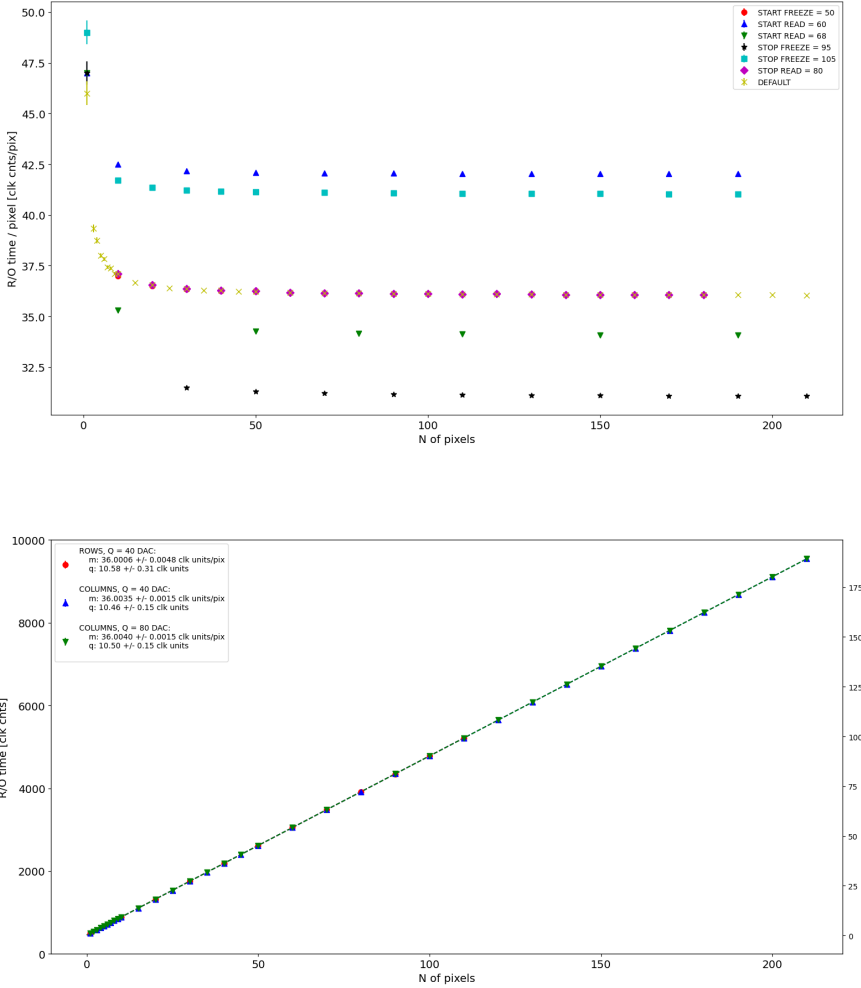


Figure 3.23: (a) Readout time per pixel as a function of the number of pixel injected obtained with different FE setup. (b) Readout time as a function of the number of pixels injected obtained injecting pulses with amplitude of 80 DAC (green), of 40 DAC on the same row (red) and on the same column (blue).

us indentifying the motivation of the break: the chip has been glued using too much conductive tape and hence have a short-circuit between the sides and the back, which makes impossible the biasing. Unfortunately, since both the sensor and the FE require at least -10 V to work properly, no measurement was possible except the acquisition of the noise in the FE circuit.

The second chip we received is a minid2, that is a "mini demonstrator" from the second submission. The two have the same charateristics but the minid2 is smaller than the MD1, in particular it only have 32×512 pixels, instead of 512×512 .

Up to now we used the injection circuit in order to make a threshold scan on a few pixels: differently from the TJ-Monopix1's charaterization where we performed a scan changing the injection charge of the pulse, with the minid2 we have instead changed the threshold (whose register is VCASN) keeping the charge of the pulse fixed. For each threshold we inject 100 pulses of amplitude $10 \mu\text{s}$. The dependence of the efficiency on the threshold for two pixels is shown in figure 3.25. Even if the behavior is reasonable, as the

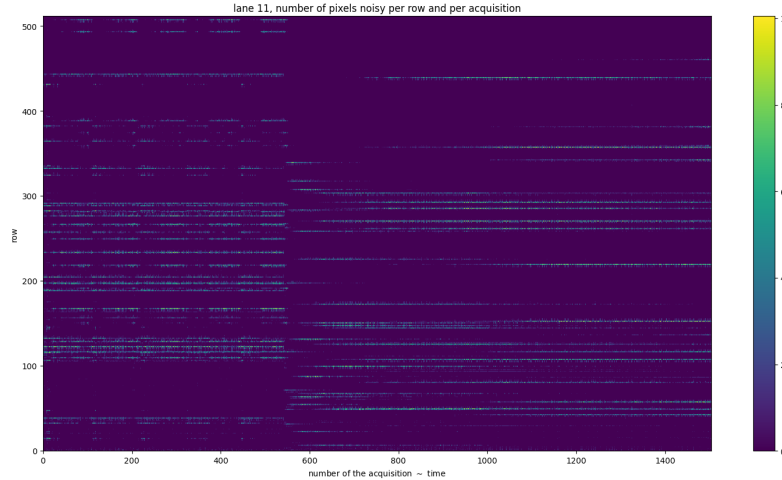


Figure 3.24: Noise in the front end circuit depending on the bias road across the matrix was recorded.

716 threshold is reduced the efficiency becomes higher, it is possible that the bias (-50 V) is not enough to full deplete the sensor, since the counts does not reach the 100% steadily.

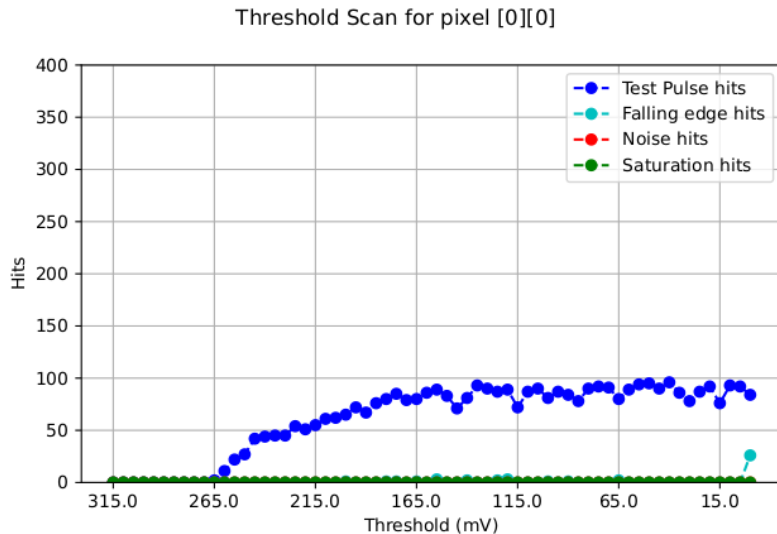


Figure 3.25: Threshold scan on the pixel (0,0). The sensors is polarized with $\Delta V = -50$ V.

717
 718 The value of the SNR and the ENC Charge injection circuit uses $C_{inj} = 2.325$ fF. The
 719 SNR, the ENC and the threshold dispersion on the matrix are expected to be respectively
 720 ~ 90 , $3 e^-$ and $\sim 35 e^-$ with a detector capacity of 7 fF, that is about the capacity expected
 721 for the detector. The injection capacity is expected to be ~ 2.325 fF, and in this condition
 722 the the minimum and maximum signals generated are respectively 0.08 fC and 2.6 fC.

723 Substantial differences have been observed with VCASN=40 DAC in both the efficiency
 724 and the threshold among the sections; this suggests that with this particular FE config-
 725 uration there is a big threshold dispersion on the matrix. The hitmap of an acquisition
 726 with the Fe55 source is shown in figure 3.26: the whole MD1 matrix with only the bottom
 727 region (32 rows) working is represented in (a), while in (b) there is a zoomed hitmap. The

728 rate seen within the region 8 (green region in the figure (a)) is compatible with the rate
of the same radioactive source measured with TJ-Monopix1, that it ~ 3.3 kHz. Looking to

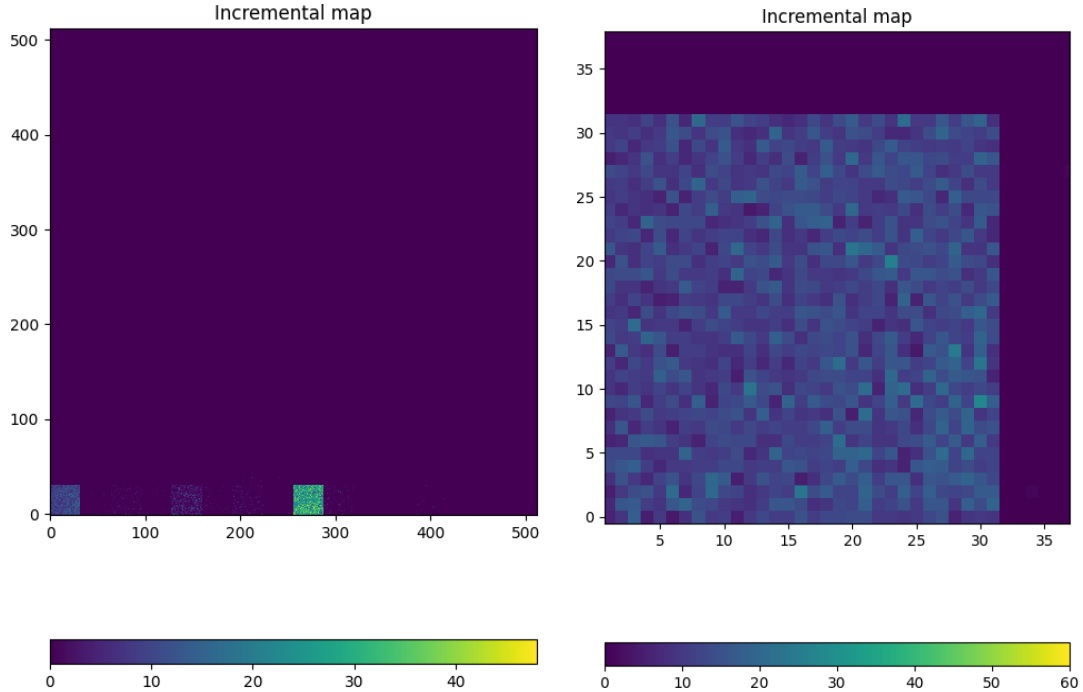


Figure 3.26: Fe55 acquisition with VCASN=40 DAC. (a) All the matrix 512×512 is plotted even if the minid2 has only the rows in range 0-32. (b) A zoom on the first section (col 0-32).

729
730 the Sr90 acquisitions (fig.3.27) many clusters and tracks can be immidiately distiguished,
confirming what observed with TJ-Monopix1.

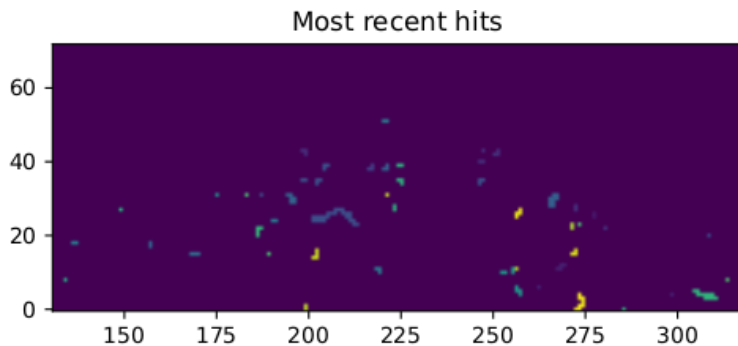


Figure 3.27: Sr90 acquisition with VCASN=40 DAC. The different colours are related with the time of arrival of the hits: in yellow the most recent hits, while in blue the old ones.

731

732 Chapter 4

733 Test beam measurements

734 During August 2022 a testbeam took place in Santa Chiara hospital in Pisa, where a
735 new accelerator designed for both medical research and R&D on FLASH-RT, and for this
736 reason called "ElectronFlash", have been installed a few months ago. The motivation
737 of the testbeam measurements were testing TJ-Mopopix1 at high dose rate with a focus
738 on investigating the possibility of the application in radiotherapy. Despite this particular
739 device does not seem fitting the requirements imposed for that application, especially
740 regarding the readout time, the measurements have been useful since help us characterizing
741 the setup for future advance, and also give us the possibility of a complete characterization
742 of the chip.

743 Given that in medical physics the dose is the standard parameter to characterize the
744 beam, because of its obvious relation with the damage caused in the patient, I am going
745 to explain the meaning of it by the point of view of the instrumentation. Infact, when
746 interacting with measuring systems a more common and useful parameter is the rate or
747 the fluence of particles. The conversion between the two quantity can be found thinking to
748 the definition of dose: it is the concentration of energy deposited in tissue as a result of an
749 exposure to ionizing radiation. Assuming total absorption of electrons in water, defined
750 by law as the ordinary reference medium, the dose can be expressed as:

$$D[Gy] = \frac{NE[eV]}{\rho[g/cm^3]A[cm^2]x[cm]} \quad (4.1)$$

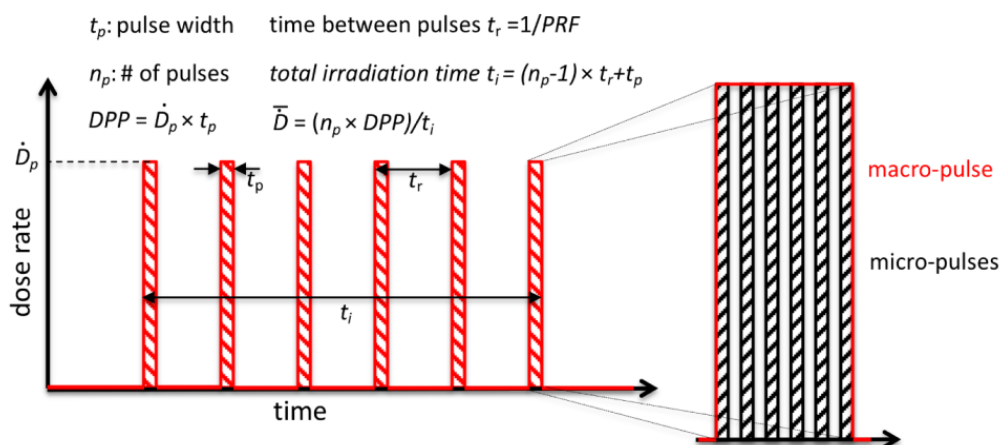


Figure 4.1: Typical beam structure of a beam used in electron radiotherapy

\bar{D}	Dose rate (mean dose rate for a multi-pulse delivery)	0.005-10000 Gy/s
\dot{D}	Intra pulse dose rate (dose rate in a single pulse)	0.01-1 10^6 Gy/s
DDP	Dose in a single pulse	0.04-40 Gy
PRF	Pulse repetition frequency	1-350 Hz
t_p	Pulse width	0.2-4 μ s
n	Number of pulses	single/pulse train

Table 4.1: The parameters that can actually be set by the control unit are the PRF, DDP, t_p and n (in particular the modality of singular irradiation or pulse train), while the other changes consequently.

751 After having applied the conversion of the energy from eV to J and noticed that $E/\rho x$
 752 roughly corresponds to the stopping power S of electrons in water, a simple estimation of
 753 the dose released in water is:

$$D[Gy] = 1.602 \cdot 10^{-10} N[cm^{-2}] S[MeV cm^2/g] \quad (4.2)$$

754 4.1 Apparatus description

755 In order to shield the outdoor from ionizing radiation the accelerator is placed in a bunker
 756 inside the hospital. The bunker has very thick walls of cementum and both the control
 757 units of the accelerator and of the detector were placed outside in a neighbor room.

758 4.1.1 Accelerator

759 The ElectronFlash accelerator is an electron Linear Accelerator (LINAC) with two energy
 760 configurations, at 7 MeV and 9 MeV, and it can reach ultra high intensity (40 Gy/pulse)
 761 keeping the possibility of accessing many different beam parameters and changing them
 762 independently from each other, a characteristic that makes it almost unique worldwide
 763 and which is fundamental for research in FLASH-RT, both for the medical aspects¹ and
 764 for the studies on detectors. The accelerator implements the standard beam structure
 765 used in RT with electrons (fig. 4.1), that is a macro pulse divided in many micropulses;
 766 the parameters used to set the dose and their range of values settable by the control unit
 767 is reported in table 4.1.

768 The accelerator is also provided of a set of triod cannons ~ 1.2 m long and with diameters
 769 in range from 1 cm to 12 cm and a collimator that can be used as beam shaper to
 770 produce a squircle shape. The triode, which is made by plexiglass, must be fix to the gun
 771 during the irradiation and is needed for producing, via the scattering of electrons with it,
 772 an uniform dose profile (fig.4.2) which is desired for medical purpose.

773 4.1.2 Mechanical carriers

774 The tested detector consists in one chip, the Device Under Test (DUT), mounted on
 775 a board and connected to FPGA with same arrangement of figure 2.3. These boards
 776 have been positioned vertically in front of the triode on a table specifically built for the

¹For example, it is not yet really clear the dependence of the efficacy of the FLASH effect on the whole beam parameters

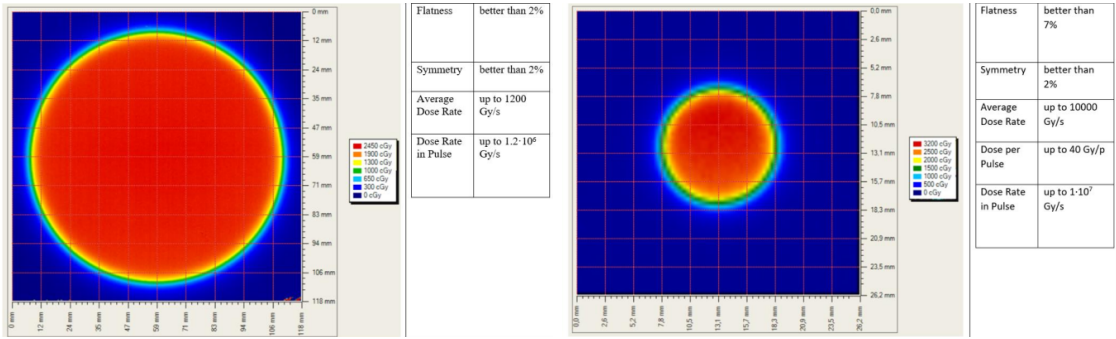


Figure 4.2: Two example of x-y isodose curves for two different triodes, 10 cm and 1 cm respectively, reported by the producer in the manual with the specific of the accelerator (S.I.T. - Sordina IORT Technologies S.p.A.). With the smaller collimator the dose rate in pulse is comparatively higher.

777 testbeam. The tree board have been enclosed in a box of alluminium with a window on
 778 the DUT and with the required holes at the side to enable the biasing via cables and the
 779 connection with the DAQ provided via ethernet cable. A trigger signal coming from the
 780 control unity and syncronized with the pulses emitted from the beam has been also sent to
 781 the FPGA. This digital signal cannot be considered a real trigger, since the TJ-Monopix1
 782 prototype has been designed to be triggerless, but its Time of Arrival (ToA) had allowed
 783 the reconstruction of the correct timing during the analysis.

784 In order to shield the sensor from the whole particles emitted from the gun, two
 785 alluminium collimators have been fabricated: one has been positioned at the triode exit
 786 while the other in front of the DUT. The collimators are $t=32$ mm thick and have a
 787 diameter d equal to 1 mm: assuming a beam divergence bigger than $d/t=1/32 = 1.8^\circ$,
 788 which is the case, the collimator at the triode output was supposed to work as a point
 789 source and to reduce the rate on the DUT of a factor at least $4 \cdot 10^{-4}$. The second one,
 790 being near the DUT, was instead supposed to shield the sensor from the electrons which
 791 have passed the first one, except for a region of 1 mm^2 configurable using **come si chiamano**
 792 **quei cacciavitini per settare la posizione? sliding trimmer?**.

793 4.2 Measurements

794 Because of the dead time of TJ-Monopix1 it is not possible resolving the bunch sub-
 795 structure and almost no one pixel can read more than a hit per bunch. I recall, indeed,
 796 that the dead time per pixel depends on the location on the readout priority chain and
 797 for each pixel $\lesssim 1 \mu\text{s}$ are needed; therefore, assuming a pulse duration of $4 \mu\text{s}$, only a few
 798 pixels at the top of the priority chain (placed at the upper left on the matrix) can fire a
 799 second time, as they can be read a first time before the end of the pulse and then can be
 800 hit again.

801 Since resolving the single electron track is impossible, a way this sensor could be used
 802 in such context is reducing its efficiency and taking advantage of the analog pile up and
 803 of the linearity of the analog output (ToT), in order to see a signal produced not by the
 804 single particle but by more electrons. Reducing the efficiency and the sensibility of the
 805 sensor is essential in order to decrease the high charge signal produced in the epitaxial
 806 layer and mitigating the saturation limit: the smaller the output signal produced by a

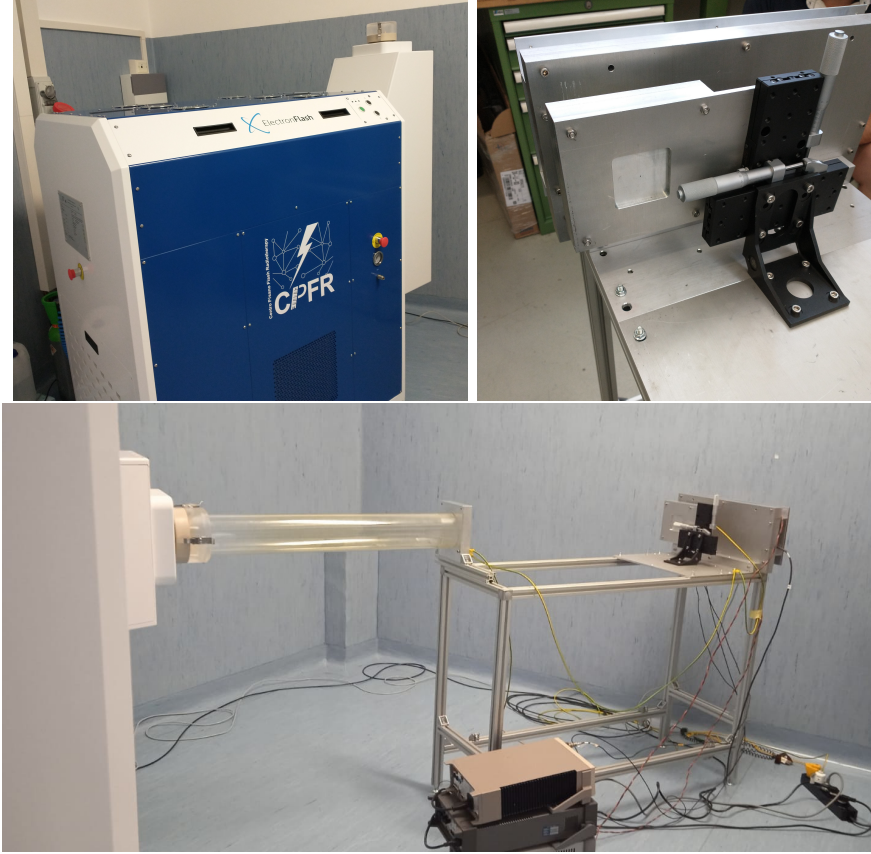


Figure 4.3: Experimental set up. (a) ElectronFlash accelerator: a rotating gantry allows the gun orientation from 0° to 90° (horizontal /vertical). (b) Collimator and DUT box. (c) Whole structure mounted: we used the 10 cm diameter and 1.2 m long triode; the DUT which is in the box behind the two collimators is connected to the power supply units.

807 particle and the higher the fluence the detector can cope with. There is an obvious limit in
 808 this context that is the ToT rollover, indeed, the signal stop giving information when this
 809 value has been overridden and is no more bijective. With the standard configuration of
 810 the FE parameters and the epitaxial layer completely depleted, a MIP produces a charge
 811 at the limit of representation with a 6-bit ToT; to obtain smaller output signals one can
 812 operate on the reduction of the gain.

813 Recalling the results in section 3.1.4, I have shown that concerning the PMOS flavor
 814 B, reducing the bias from -6 V to 0 V brings a reduction of efficiency down to 40 %, and a
 815 reduction in the gain of a factor $\sim 1/3$, while the reduction of the gain of the preamplifier
 816 allows a reduction of **circa 10, ma da controllare**.

817 In order to take advantage of the analog pile up and integrating the charge, for
 818 simplicity assume of two electrons, the second one must hit the pixel before the ToT goes
 819 under the threshold. The general condition is then $\overline{\Delta T} < \overline{ToT}$, but if a high $P_\mu(n \geq 1)$ is
 820 required, a lower $\overline{\Delta T}$ may be desired:

$$P(n \geq 1) = \sum_{n=1}^{\infty} \frac{e^{-\mu} \mu^n}{n!} = 1 - P(0) = 1 - e^{-\mu} \quad (4.3)$$

821

$$\mu = \frac{\overline{ToT}}{\overline{\Delta T}} \quad (4.4)$$

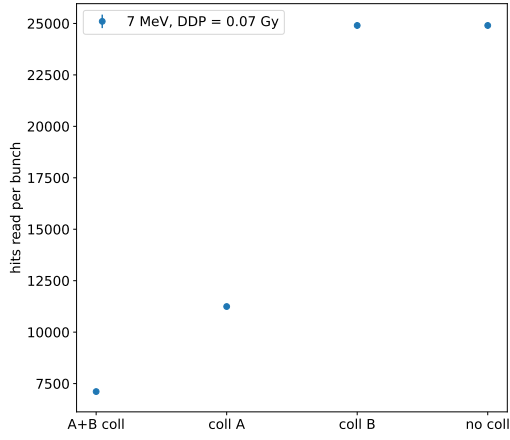


Figure 4.4: Mean number of hits read per bunch at DDP=0.07 Gy, with all the possible setup condition: with both the collimator, with only the collimator far from the chip (A), with only the collimator near the chip (B), and without any collimator.

822 If a $P_\mu(n \geq 1) = 99\%$ then the $\overline{\Delta T}$ must be $\sim 0.22 \overline{ToT}$. The ToT is in range [0,64] but
 823 since the rollover must be avoided, the \overline{ToT} must be lower than 32, and then the minimum
 824 rate on the pixel must be 1.25 MHz.

825
 826 During the testbeam many runs have been performed, spanning the energy, the dose
 827 per pulse and the four possible configurations with/without the collimators. We have
 828 collected data with the PMOS flavor A in the standard configuration: with the PWELL
 829 and PSUB biased at -6 V and set the standard default FE parameters reported in table
 830 ???. During all the data acquisitions we have selected on the control unit of the accelerator
 831 pulses with t_p of 4 μ m and with the smallest PRF settable, which is 1 Hz, in order to start
 832 in the most conservative working point excluding the digital pile up of events from different
 833 bunches. In these conditions, even if the whole matrix turns on, the total readout time
 834 corresponds to $25000 \times 1 \mu s = 25 \text{ ms}$ is still lower than the time between two consecutive
 835 pulses. In figure 4.4 is shown the mean number of hits read during one accelerator pulse
 836 in different setup conditions.

837 The readout starts with the trailing edge of the first pulse going down the threshold:
 838 about 50 clk=1.25 μ s after this moment the FREEZE signal is sent to the whole matrix,
 839 and the transmission of the data to the EoC begins. The hits read during the FREEZE
 840 signal are the ones whose TE occurred before the start of the FREEZE and which have the
 841 TOKEN signal high; the ones, instead, whose TE occur during the FREEZE are stored in
 842 the pixel memory until the end of the FREEZE. At this point a second readout starts and
 843 a second FREEZE is sent to the matrix. An example of the two sub-pulses corresponding
 844 to an electron bunch is shown in figure 4.5: in the acquisition we injected 5 pulses with
 845 both the collimators mounted on the table. Looking at the spectrum we can see that the
 846 second sub-pulse has a populated tail on the right; this is due to the fact that the hits
 847 which arrive before the start of the first FREEZE but have a long ToT that falls during
 848 the FREEZE, are read at the second sub-pulse.

849 The 2D histograms in figure 4.5, reveal an important characteristics of our setup: in

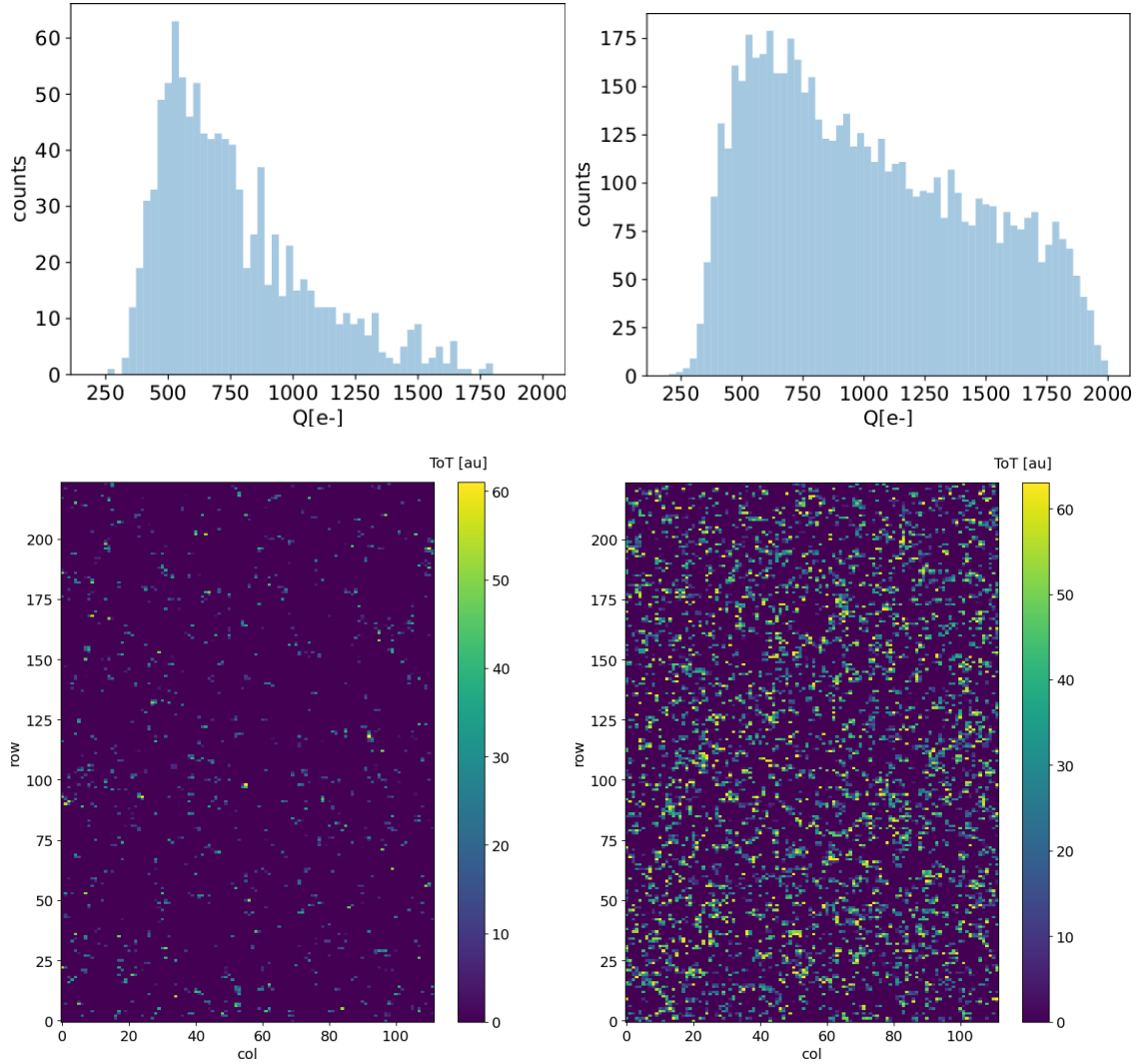


Figure 4.5: Acquisition with both the collimators: 5 pulses at $DDP=0.07\text{ Gy}$. (a) Spectrum of the charge released in the sensor: to apply the conversion I used the information found in the previous chapter. (b) 2D histogram of the ToT of the hits arrived in the sub-pulses.

fact, being uniform and not showing disomogenities, it follows that the collimators do not shield all the particles. We supposed that this was due to a Bremsstrahlung photon background higher than expected but a full verification of that and the analysis of the data is still going on. In figure 4.6, instead, the histograms with a higher DDP value is shown; in the example the matrix turns on completely, but again this happens in two different consecutive read chain.

When we have put aside the collimators, instead, the fluence increase a lot and the two-pulses substructure no more appears (fig. 4.7), but, because of the high attivity of the matrix, after each readout new hits with a fixed ToT were induced due to crosstalk. This problem had already been observed on other prototypes of TJ-Monopix1, and thanks to a simulation it has been observed that the main source of crosstalk is the voltage drop of the pre-amplifier ground as a result of the accumulated current that is drawn from the discriminator.

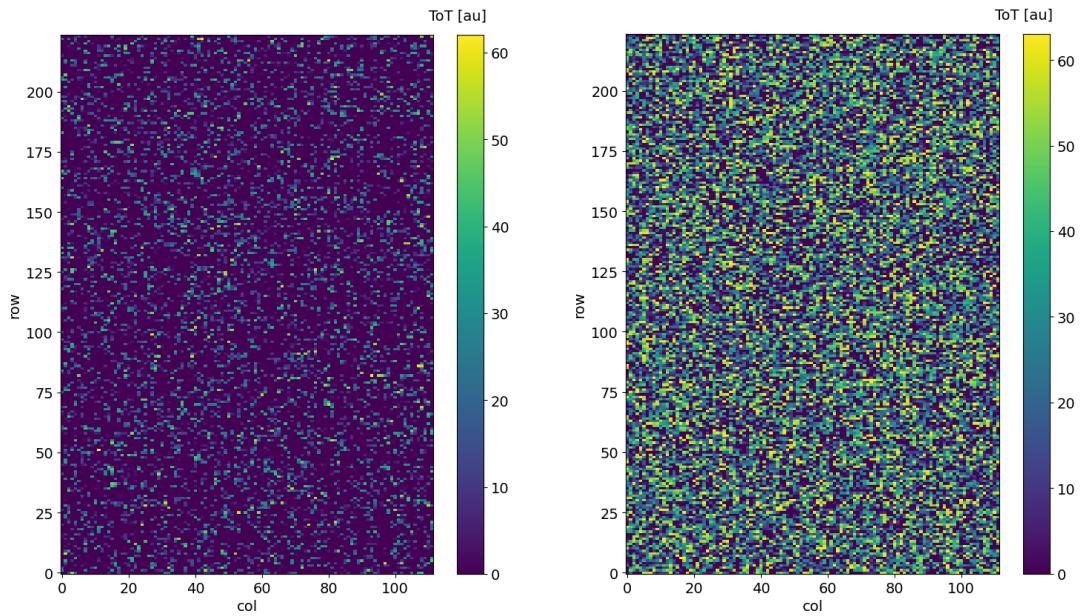


Figure 4.6: Acquisition with both the collimators: 5 pulses at DDP=0.6 Gy. 2D histogram of the ToT of the hits arrived in the sub-pulses. Compared with the previous maps, since the DDP is much higher, more pixels turn on.

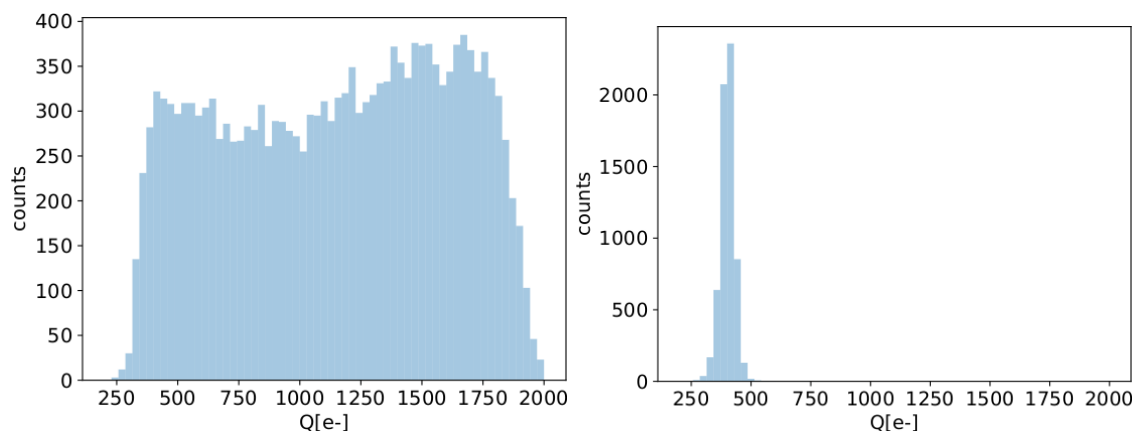


Figure 4.7: Acquisition without any collimator: 5 pulses at DDP=0.04 Gy.

863 Bibliography

- 864 [1] W. Snoeys et al. “A process modification for CMOS monolithic active pixel sensors
865 for enhanced depletion, timing performance and radiation tolerance”. In: (2017).
866 DOI: <https://doi.org/10.1016/j.nima.2017.07.046>.
- 867 [2] H. Kolanoski and N. Wermes. *Particle Detectors: Fundamentals and Applications*.
868 OXFORD University Press, 2020. ISBN: 9780198520115.
- 869 [3] E. Mandelli. “Digital Column Readout Architecture for 10.1109/NSSMIC.2009.5402399
870 the ATLAS Pixel 0.25 um Front End IC”. In: (2002).
- 871 [4] M. Garcia-Sciveres and N. Wermes. “A review of advances in pixel detectors for
872 experiments with high rate and radiation”. In: (2018). DOI: <https://doi.org/10.1088/1361-6633/aab064>.
- 874 [5] C. Marinas. “The Belle-II DEPFET pixel detector: A step forward in vertexing in the
875 superKEKB flavour factory”. In: (2011). DOI: [doi:10.1016/j.nima.2010.12.116](https://doi.org/10.1016/j.nima.2010.12.116).
- 876 [6] J. Baudot. “First Test Results Of MIMOSA-26, A Fast CMOS Sensor With Inte-
877 grated Zero Suppression And Digitized Output”. In: (2010). DOI: [doi:10.1109/NSSMIC.2009.5402399](https://doi.org/10.1109/NSSMIC.2009.5402399).
- 879 [7] A. Dorokhov. “High resistivity CMOS pixel sensors and their application to the
880 STAR PXL detector”. In: (2011). DOI: [doi:10.1016/j.nima.2010.12.112](https://doi.org/10.1016/j.nima.2010.12.112).
- 881 [8] Giacomo Contin. “The STAR MAPS-based PiXeL detector”. In: (2018). DOI: <https://doi.org/10.1016/j.nima.2018.03.003>.
- 883 [9] Nolan Espplen. “Physics and biology of ultrahigh dose-rate (FLASH) radiotherapy:
884 a topical review”. In: (2020). DOI: <https://doi.org/10.1088/1361-6560/abaa28>.
- 885 [10] Fabio Di Martino et al. “FLASH Radiotherapy With Electrons: Issues Related to
886 the Production, Monitoring, and Dosimetric Characterization of the Beam”. In:
887 *Frontiers in Physics* 8 (2020). ISSN: 2296-424X. DOI: [10.3389/fphy.2020.570697](https://doi.org/10.3389/fphy.2020.570697).
888 URL: <https://www.frontiersin.org/articles/10.3389/fphy.2020.570697>.
- 889 [11] M. Dyndal et al. “Mini-MALTA: Radiation hard pixel designs for small-electrode
890 monolithic CMOS sensors for the High Luminosity LHC”. In: (2019). DOI: <https://doi.org/10.1088/1748-0221/15/02/p02005>.
- 892 [12] M. Barbero. “Radiation hard DMAPS pixel sensors in 150 nm CMOS technology
893 for operation at LHC”. In: (2020). DOI: <https://doi.org/10.1088/1748-0221/15/05/p05013>.
- 895 [13] K. Moustakas et al. “CMOS Monolithic Pixel Sensors based on the Column-Drain
896 Architecture for the HL-LHC Upgrade”. In: (2018). DOI: <https://doi.org/10.1016/j.nima.2018.09.100>.

- 898 [14] I. Caicedo et al. “The Monopix chips: depleted monolithic active pixel sensors with
899 a column-drain read-out architecture for the ATLAS Inner Tracker upgrade”. In:
900 (2019). DOI: <https://doi.org/10.1088/1748-0221/14/06/C06006>.
- 901 [15] D. Kim et al. “Front end optimization for the monolithic active pixel sensor of the
902 ALICE Inner Tracking System upgrade”. In: *JINST* (2016). DOI: doi:10.1088/
903 1748-0221/11/02/C02042.
- 904 [16] L. Pancheri et al. “A 110 nm CMOS process for fully-depleted pixel sensors”. In:
905 (2019). DOI: <https://doi.org/10.1088/1748-0221/14/06/c06016>.
- 906 [17] L. Pancheri et al. “Fully Depleted MAPS in 110-nm CMOS Process With 100–300-
907 um Active Substrate”. In: (2020). DOI: 10.1109/TED.2020.2985639.